

MICCAI 2013

NAGOYA JAPAN

SEP. 22-26, 2013

TOYODA AUDITORIUM
NAGOYA UNIVERSITY



MICCAI-STENT

The 2nd MICCAI-Workshop on Computer Assisted Stenting

MICCAI, 22.September 2013
Nagoya, Japan

<http://campar.in.tum.de/STENT2013/WebHome>

Preface

This workshop aims to bring together scientific researchers and medical experts in the field of endovascular stenting procedures in different anatomical regions. While researchers concerned with cerebral, coronary, carotid, and aortic stenting have mostly published within their corresponding anatomy, the MICCAI-STENT workshop will provide a platform for scientific discussion on stent-related research across anatomical boundaries. The aim is to form the basis of a specialized subcommunity within MICCAI.

The workshop will focus on imaging, treatment and computed assisted technological advances in diagnostic and intraoperative imaging. Such techniques offer increasingly useful information regarding vascular anatomy and function and are poised to have dramatic impact on the diagnosis, analysis, modeling, and treatment of vascular diseases. Computational vision techniques designed to analyze images for modeling, simulating, and visualizing anatomy and medical devices such as stents as well as the assessment of interventional procedures are therefore playing an important role and are currently receiving significant interest.

August 2013

Simone Balocco
Carlo Gatta
Stefanie Demirci
Su-Lin Lee
Geir Arne Tangen

Workshop Commitee

Steering Committee

Ignacio Larrabide, PhD, University Pompeu-Fabra, Spain

Nassir Navab, CAMP/TUM, Germany

Gozde Unal, PhD, Sabanci University, Turkey

Petia Radeva, PhD, Universitat de Barcelona, Spain

Technical Board

Georg Langs, Medical University Vienna, Austria

Ying Zhu, Siemens Corporate Research, US

Regis Vaillant, General Electric, France

Nenad Filipovic, University of Kragujevac, Serbia

Francesco Ciompi, PhD, Autonomous University of Barcelona, Spain

Maria Alejandra Zuluaga, PhD, University College London, UK

Razvan Ionasec, Siemens Corporate Research, US

Medical Board

Frode Manstad-Hulaas, MD, St. Olavs Hospital, Norway

Dr. Christian Loewe, Medizinische Universität Wien, Austria

Dr. Hans-Henning Eckstein, Klinikum rechts der Isar, Germany

Dr. Reza Ghotbi, Kreisklinik Muenchen-Pasing, Germany

Dr. Christian Reeps, Klinikum rechts der Isar, Germany

Contents

1. 3D/3D Registration of Coronary CTA and Biplane XA Reconstructions for Improved Image Guidance
Gerardo Dibildox, Mark Punt, Jean-Paul Aben, Carl Schultz, Wiro Niessen and Theo van Walsum
2. Visualization of stent-graft placement in deformed vascular structure in EVAR procedure
Aurélien Duménil, Adrien Kaladji, Juliette Gindre, Miguel Castro, Michel Rochette, Cemil Göksu, Antoine Lucas and Pascal Haigron
3. *Invited speaker* : Learning-based Modeling of Endovascular Navigation for Collaborative Robotic Catheterization
H. Rafii-Tari, J. Liu, S.-L. Lee, G.-Z. Yang
4. *Invited speaker* : Stent shape estimation through a comprehensive interpretation of ivus image
Francesco Ciompi, Simone Balocco, Carles Caus, Josepa Mauri, Petia Radeva
5. Augmented Reality Guidance System for Transcatheter Aortic Valve Implantation
Jonathan McLeod, Maria Currie, John Moore and Terry Peters
6. Automatic Flow Diverter Detection in Submission Cerebral C-arm CT Images
Ying Zhu et al.
7. Investigation of Hemodynamics in a Large Unruptured Intracranial Aneurysm Using Computational Fluid Dynamics Technique
Wen Liu, Lin Shi, Tianfu Wang, Defeng Wang and Simon Yu
8. Development of a System for Endovascular Planning of AAA Interventions
Ivan Macia, Jon Hartz Legarreta, Sabarinath Rajasekharan, Elena Muñoz, Oscar Hernandez, Mariano De Blas Bravo, Jose Maria Egaña and Manuel Graña

3D/3D Registration of Coronary CTA and Biplane XA Reconstructions for Improved Image Guidance

Gerardo Dibildox^{1,2}, Mark Punt³, Jean-Paul Aben³, Carl Schultz⁴, Wiro Niessen^{1,2,5}
and Theo van Walsum^{1,2}

¹ Department of Radiology, Erasmus MC, Rotterdam, The Netherlands

² Department of Medical Informatics, Erasmus MC, Rotterdam, The Netherlands
g.dibildox@erasmusmc.nl

³ Pie Medical Imaging, Maastricht, The Netherlands

⁴ Department of Cardiology, Erasmus MC, Rotterdam, The Netherlands

⁵ Delft University of Technology, Delft, The Netherlands

Abstract. We present and evaluate a method for registering pre-operative coronary CTA with intraoperative biplane X-ray angiography images via 3D models of the coronary arteries. The models are extracted from the CTA and biplane images and are temporally aligned based on the CT reconstruction phase and ECG signals. Spatial alignment is done with a robust probabilistic point set approach in a rigid manner. Evaluation of our registrations using clinical data and their projections to the XA imaging planes show results on the order of 1mm and sub-millimeter in several cases indicating the potential for integrating CTA information for improved image guidance.

Keywords. Image guidance, 3D/3D registration, CTA, biplane reconstruction, chronic total occlusions

1 Introduction

Percutaneous coronary intervention (PCI) is a minimally invasive procedure for patients with advanced coronary artery disease. PCI involves the introduction of a guiding catheter via arterial access and the use of a guidewire and balloon or stent catheter to cross a stenosis and deploy a stent at the lesion site. Visualization during PCI is achieved by means of X-ray angiography (XA). High success rates have been reported for normal PCI [1], but patients with a chronic total occlusion (CTO) remain a difficult subset of patients to treat with PCI [2] due to the complete nature of their stenosis, which results in the absence of contrast flow and therefore the visualization of the occluded segment during the intervention. These patients could potentially benefit from improvements in the image guidance of the intervention.

The integration of preoperative with intraoperative imaging is a known strategy in image guidance and work has been done, for example, in fusing preoperative magnetic resonance imaging to X-ray fluoroscopy to guide the recanalization of peripheral artery CTOs [3]. There have also been attempts to provide additional visual information to the cardiac interventionist treating CTO's by integrating preoperative CTA -

the occluded segment can usually be seen on cardiac CT - with intraoperative X-ray images by aligning 3D and 4D CTA with 2D X-ray image sequences [4][5][6].

The purpose of our work is to develop and evaluate a method that does a similar registration based on two 3D models obtained from 3D CTA and biplane X-ray Angiography (XA). Biplane imaging is the preferred visualization for complex lesions such as CTOs. Utilizing a direct 3D-3D registration may facilitate the registration, and also allows us to investigate the differences in coronary shapes between reconstructions from pre-operative CTA and biplane XA. For the registration method we prefer a density-based approach [7] to align the pre-operative model to the interventional reconstruction over a point-based ICP approach. Main contributions of our work are the development of an integrated method to do a 3D-3D registration for aligning CTA and XA images in the context of PCI and an evaluation of the approach w.r.t. accuracies and robustness to the initial alignment. Furthermore, our method facilitates a quantitative evaluation of shape differences between centerline models obtained from pre-operative imaging data versus centerline models obtained from interventional imaging data.

2 Method

Below, we describe the biplane reconstruction method, the construction of the 3D CTA centerline model, and the temporal and spatial alignment of these two models.

2.1 Biplane XA Reconstructions

Input for the biplane reconstructions are the coronary artery centerlines that are obtained from XA images. The system geometry is established with the information provided in the DICOM tags. Subsequently, an adaptive 3D epipolar geometry algorithm is used to reconstruct a 3D centerline model taking into account system distortion introduced by the isocentre offset [8]. In case a 3D reconstruction cannot be created from the XA images, an interpolation from the 3D reconstructions of adjacent frames is performed. The XA sampling rate is known and the ECG data is available for each image.

2.2 CTA Centerlines

CTA centerlines of the coronary arteries are extracted from CTA using a minimum cost path approach algorithm [9]. To this end, the following cost image is generated from a CTA image:

$$C(\vec{x}, \sigma) = \frac{1}{V(\vec{x})I(\vec{x}, \sigma) + \varepsilon} \quad (1)$$

where V is a Frangi-based vesselness measure, I an intensity measure and ε a small positive value to avoid singularity of the function.

Subsequently, a starting point in the ostium of the coronary artery, and endpoints of the left and right coronary tree are manually input, after which the coronary artery centerlines are extracted via a minimum cost path search. Accuracy of the minimum cost path algorithm has been reported [9] to be between 0.5-0.65mm for the average distance between extracted centerlines and a reference standard.

2.3 Alignment of 3D CTA and Biplane XA Reconstructions

Temporal alignment. As the heart changes shape over the cardiac cycle, temporal alignment, i.e. building both 3D models from the same cardiac phase, is essential for optimal alignment. Nowadays it is common to use prospective gating in cardiac CTA: imaging only a part of each cardiac cycle. We therefore choose the CTA cardiac phase as the phase for alignment, which typically is around 70% of the R-R cycle.

The biplane XA images selected for the reconstructions in our experiments cover one complete R-R cycle at a known sampling rate. The ECG information stored in the XA DICOM tags is used to select the images that correspond to the phase of the CTA model.

Spatial Alignment. The phase matched 3D model from CTA and biplane XA are represented as a set of points along the centerlines, i.e. let $\{C, B\}$ be two finite size point sets, where C represents the points describing the CTA extracted centerlines and B the points of the biplane reconstruction. In the registration process, these models are interpreted as probability density functions, and registration is performed, which allows them to be registered using the approach by Jian and Vemuri [7]. This method minimizes the L2 distance metric between two probability density functions:

$$d_{L_2}(B, C, \theta) = \int (gmm(B) - gmm(T(C, \theta)))^2 dx \quad (2)$$

where $gmm(P)$ refers to the Gaussian mixture model of point set P and θ are the parameters of the spatial transformation family T . This approach does not require explicit point correspondence and therefore is less sensitive to outliers and missing information. The initial orientation of the point sets was based on the coordinate system of the biplane system and the initial positioning was performed by aligning the centers of mass of the reconstructions, such that the models were approximately oriented similarly and positioned close to each other. The algorithm assumes no prior information and each of the Gaussian components in the Gaussian mixture models corresponds to a point in the point sets. In the current work, all points are equally weighted and all share the same spherical covariance matrix. Additionally, we assume no deformation, so a 6-degrees-of-freedom rigid transform is used.

3 Experiments and Results

The method has been applied to retrospectively acquired clinical data. We performed experiments to evaluate the registration accuracy and convergence, and the effect of using off-phase coronary reconstructions, and also to investigate the shape

differences between the 3D coronary models. Below, we first discuss the data, followed by a description of the experiments and the results.

3.1 Imaging data and pre-processing

We retrospectively acquired coronary CTA datasets for 9 CTO patients. For these datasets the centerlines of the right (3) or left (6) coronary tree were extracted using the centerline extraction minimum cost path approach. For all patients the CT data was acquired on a Siemens SOMATOM Definition Flash scanner. The field of view used for the CT reconstructions was 512x512 with a voxel size of approximately $0.35 \times 0.35 \times 0.45 \text{ mm}^3$. The slice thickness used for reconstructing the individual slices was 0.75 mm and the average number of slices for all datasets was 303. Median heart rate during the CTA scans was 65 bpm (37-96), for all except one patient the reconstruction phase was around 75 % of the cardiac cycle.

These patients had also undergone a percutaneous coronary intervention with a Siemens AXIOM-Artis biplane system. The XA images contain 1024×1024 pixels with a pixel size of either $0.139 \times 0.139 \text{ mm}^2$ or $0.184 \times 0.184 \text{ mm}^2$. The biplane image sequences were used for the biplane reconstructions of the coronary arteries featuring the CTO's over one heart cycle (R-R interval) for each patient. Median length of one cardiac cycle was 15 frames (11-18). The XA imaging frequency was 15 Hz for all patients. XA frames covering an R-R interval were selected by visually inspecting the images for presence of contrast agent and the vessels proximal and distal to the CTO were manually annotated and then reconstructed in 3D for each frame. Median heart rate during XA was 63 bpm (50-82), median heart rate difference between XA and CTA was 10 bpm (2-25).

3.2 Registration Experiments

We performed 3 sets of experiments.

In the first experiment we investigate the feasibility and accuracy of alignment of CTA extracted centerlines with phase matched biplane reconstructions using the Gaussian mixture model approach. To this end we performed 27 3D rigid point set registrations. With each patient having multiple biplane reconstructions covering the R-R interval we selected the 3 frames with the phase closest to the CTA reconstruction phase of the CTA extracted centerlines and performed the registration on these.

Additionally, to test the premise that using phase information results in the temporally alignment of our models we investigated the effect of using off-phase models in the registration. Therefore we performed an off-phase rigid point set registration for each patient where we registered the CTA extracted centerlines to the biplane reconstructions at systole (10% of the R-R interval).

To test the capture range of the registration we also perturbed the initial alignment of the CTA extracted centerlines with the phase matched biplane reconstruction by applying a rotation to the CTA extracted centerlines of ± 5 and 10 degrees. Rotation was performed by rotating the CTA extracted point sets around their center of mass along the axis pointing from patient posterior to patient anterior, patient right to pa-

tient left and patient head to patient feet. A registration was considered successful if the final 2D distance metric was less than 1.5 mm, which is less than a coronary artery radius.

In order to evaluate the registrations we calculate a mean distance (and the standard deviation) between the two 3D point sets before and after registration. Additionally, we quantify a similar metric after projection of the CTA centerlines to the XA images, to investigate the use of our approach for improving image guidance.

3.3 Implementation

The biplane reconstructions consist of 3D point sets depicting the coronary artery proximal and distal to the CTO with one or more visible branches when possible. Hence, only centerlines corresponding to this vasculature were taken from the CTA extracted centerlines for the registration. The 3D reconstructions of the biplane intraoperative X-ray images are performed using QCA3D within CAAS 5v11 (Pie Medical Imaging, the Netherlands). The Gaussian mixture model registration approach is more robust when pairs of point sets are of similar sampling rates and therefore the biplane reconstructions and CTA extracted centerlines were resampled equidistantly at a distance of 0.25mm. This resulted in CTA extracted point sets with an average of 685 points per set and biplane reconstruction point sets with an average of 429 points per set. Initialization of the point sets required a simple transformation (rotation) to account for the different coordinate systems used in the CTA and biplane reconstructions and a translation based on their centers of mass. The registration was done with the GMMREG algorithm developed by Jian and Vemuri (downloadable at <http://gmmreg.googlecode.com>).

Evaluation in 3D was performed by calculating distances between closest corresponding points. Evaluation in 2D was performed in the same manner after projecting the CTA registered model and biplane reconstruction to the image plane.

3.4 Results

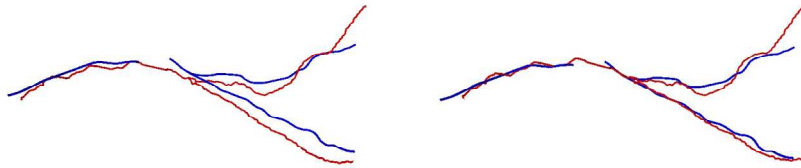


Fig. 1. Shows a CTA extracted centerline and a biplane reconstruction before and after registration.

The results of the first experiments are in Table 1, which lists the mean distance and standard deviation between CTA extracted centerlines and biplane reconstructions for

the phase matched and off phase experiments as well as an initial alignment distance. An example registration is shown in Fig.1.

Table 1. Contains mean distance and standard deviation before and after registration of phase matched and off phase registration experiments. The Initial distance is based on the mean distance between the initial alignment of the CTA extracted centerlines with the second phase matched frame, before registration.

Patient	Initial (mm)	Phase Matched 1 (mm)	Phase Matched 2 (mm)	Phase Matched 3 (mm)	Off phase (mm)
1	2.7 ± 3.2	0.7 ± .9	1.0 ± 1.5	1.4 ± 2.2	1.6 ± 1.3
2	4.5 ± 1.9	1.0 ± 1.3	1.5 ± 1.2	1.8 ± 1.3	2.0 ± 2.4
3	20.1 ± 0.8	0.2 ± 0.7	1.3 ± 0.8	1.4 ± 0.8	0.4 ± 1.5
4	5.8 ± 1.0	2.1 ± 0.7	1.4 ± 0.8	1.4 ± 0.7	1.5 ± 0.7
5	4.4 ± 2.8	1.9 ± 1.4	1.8 ± 1.2	3.2 ± 2.2	2.0 ± 1.7
6	7.4 ± 7.7	2.6 ± 3.6	5.5 ± 9.3	2.5 ± 3.2	1.8 ± 3.0
7	3.9 ± 3.2	0.9 ± 1.0	0.7 ± 0.7	0.8 ± 0.7	1.9 ± 2.8
8	3.2 ± 2.0	1.3 ± 1.3	1.2 ± 1.1	1.0 ± 1.0	0.7 ± 0.7
9	4.2 ± 4.8	0.9 ± 1.0	0.7 ± 1.0	23.1 ± 22.3	0.7 ± 0.9
Median	4.4 ± 2.8	1.0 ± 1.3	1.3 ± 0.8	1.4 ± 0.8	1.6 ± 1.3

In the capture range experiment initialization is perturbed by +/- 5 and 10 degrees around each axis (x,y,z) for the 9 patients resulting in 108 (4*3*9) registrations. 93 out of the 108 registrations were consistent with their unperturbed initial registration. Only 15 of the 108 registrations went from an initially successful registration (1.5mm criterion) in the unperturbed experiment to a failed registration in the capture range test. For the two patients with unsuccessful initial registrations, the capture range test also returned failed registrations.

Projecting the 3D registered CTA centerlines and a set of phase matched biplane reconstructions to the XA image plane of each C-arm of the biplane system resulted in 2D distance metrics with a median value of 1.2 ± 1.0mm. Of the 18 projections 7 were measured to be at sub-millimeter accuracy, results ranged from 0.2 ± 0.2mm to 5.6 ± 3.8mm. An example of a projection is shown in figure 2.

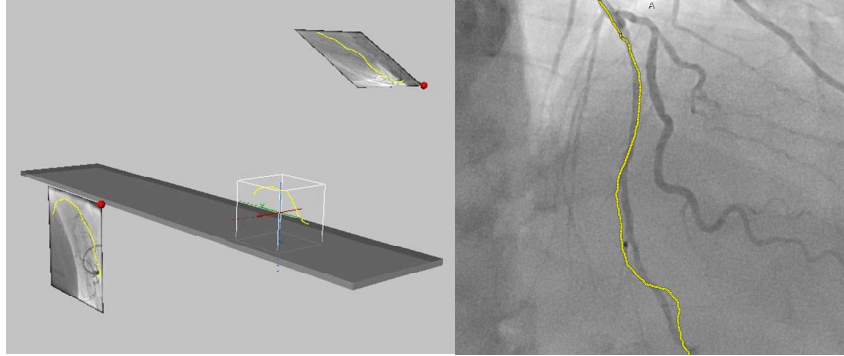


Fig. 2. Projection of registered CTA centerline to XA image planes and a resulting overlay

4 Discussion and Conclusion

We presented and evaluated a method to align CTA to biplane angiography images, by registering two 3D centerline models that were obtained from the CTA and biplane XA images. The results show that we are able to align preoperative coronary CTA data with intraoperative biplane X-ray angiography using a robust probabilistic registration approach. Average distances between registered centerlines are on the order of 1mm with several registrations achieving sub-millimeter accuracy. The 2D error measures are slightly better than those reported in [5], [6] and [10] but direct comparison is hard, as we evaluate on different datasets.

As expected, registrations of the phase matched centerlines tend to outperform the off-phase matched experiments except when there is a failed registration or the patient had a large difference in heart rate. Failure of registration was attributed to severe shape mismatch between the CTA and XA reconstructions such as for centerlines featuring different bifurcations. One other failure could be attributed to the biplane reconstruction not being a proper subset of the CTA extracted centerlines. One patient had only a small portion of the coronary artery visible in the XA image, resulting in a small reconstruction evidenced by an atypically large initial distance and very good yet meaningless registration results. Perturbation of the initial alignment proved stable in most cases. The registration itself takes about 1 second.

We are considering several improvements of the registration method, e.g. including reconstruction accuracies in the GMM covariance matrices, including more vessels in the point sets and giving the bifurcations extra weight in the algorithm as they are potentially better landmarks. Non-rigid registration methods should also be explored as a way to deal with deformations [11][12], such as those introduced by the guidewire during the intervention. Future work will furthermore include evaluation on a larger set of patient data, and analyzing the differences in cardiac shape during CTA and XA for different heart rates and development of real-time biplane reconstruction.

In conclusion, we developed a method that performs registration on two 3D models obtained by pre-operative CTA and intraoperative biplane X-ray angiography and demonstrated the applicability of the approach.

References

1. SV Rao, F Ou, TY Wang, et al. Trends in the Prevalence and Outcomes of Radial and Femoral Approaches to Percutaneous Coronary Intervention: A Report From the National Cardiovascular Data Registry. *J Am Coll Cardiol Interv.* 2008;1(4):379-386.
2. S Rathore, H Matsuo, M Terashima, et al. Procedural and In-Hospital Outcomes After Percutaneous Coronary Intervention for Chronic Total Occlusions of Coronary Arteries 2002 to 2008: Impact of Novel Guidewire Techniques. *J Am Coll Cardiol Interv.* 2009;2(6):489-497.
3. A.J. Klein, M.T. Tomkowiak, K.K. Vigen, T.A. Hacker, M.A. Speidel, M.S. van Lysel, N. Shah, A.N. Raval, Multimodality image fusion to guide peripheral artery chronic total arterial occlusion recanalization in a swine carotid artery occlusion model: Unblinding the interventionalist, *Catheterization and Cardiovascular Interventions* Volume 80, Issue 7, pages 1090–1098, December 2012
4. D. Ruijters, B. M. ter Haar Romeny, and P. Suetens, “Vesselness-based 2D–3D registration of the coronary arteries,” *International Journal of Computer Assisted Radiology and Surgery*, vol. 4, no. 4, pp. 391–397, May 2009.
5. C.T. Metz, M. Schaap, S. Klein, P. Rijnbeek, L. Neefjes, N.R.A. Mollet, C. Schultz, P.W. Serruys, W.J. Niessen and T. van Walsum, Alignment of 4D Coronary CTA with Monoplane X-Ray Angiography, 6th International Workshop, AE-CAI 2011, Held in Conjunction with MICCAI 2011 , 2011
6. N. Baka, C.T. Metz, C. Schultz, L. Neefjes, R.J. van Geuns, B.P.F. Lelieveldt, W.J. Niessen, M. de Bruijne and T. van Walsum, 3D+t/2D+t CTA-XA registration using population-based motion estimates, *MICCAI-Workshop on Computer Assisted Stenting Proceedings, MICCAI-STENT'12* , 2012
7. B. Jian and B. Vemuri. Robust Point Set Registration Using Gaussian Mixture Models, *Pattern Analysis and Machine Intelligence*, IEEE Transactions on, Aug. 2011
8. J. C. H. Schuurbijs, N. G. Lopez, J. Ligthart, F. J. H. Gijsen, J. Dijkstra, P. W. Serruys, A. F. Van der Steen, and J. J. Wentzel, “In vivo validation of CAAS QCA-3D coronary reconstruction using fusion of angiography and intravascular ultrasound (ANGUS),” *Catheterization and Cardiovascular Interventions*, vol. 73, no. 5, pp. 620–626, Apr. 2009.
9. C.T. Metz, M. Schaap, A.C. Weustink, N.R.A. Mollet, T. van Walsum and W.J. Niessen, Coronary centerline extraction from CT coronary angiography images using a minimum cost path approach, *Medical Physics*, 2009
10. J. Hadida, C. Desrosiers, and L. Duong, “Stochastic 3D Motion Compensation of Coronary Arteries from Monoplane Angiograms,” in *Medical Image Computing and Computer-Assisted Intervention – MICCAI 2012*, vol. 7510, N. Ayache, H. Delingette, P. Golland, and K. Mori, Eds. Berlin, Heidelberg: Springer Berlin Heidelberg, 2012, pp. 651–658.
11. E. Serradell, A. Romero, R. Leta, C. Gatta and F. Moreno-Noguer, “Simultaneous correspondence and non-rigid 3D reconstruction of the coronary tree from single X-ray images,” in *Computer Vision (ICCV), 2011 IEEE International Conference on*. IEEE 2011.
12. M. Groher, D. Zikic and N. Navab, “Deformable 2D-3D registration of vascular structures in a one view scenario,” *Medical Imaging, IEEE Transactions on*, 28.6 (2009): 847–860.

Visualization of stent-graft placement in deformed vascular structure in EVAR procedure

Aurélien Duménil^{1,2,3}, Adrien Kaladji^{1,2,4}, Juliette Gindre^{1,2}, Miguel Castro^{1,2}, Michel Rochette⁵, Cemil Göksu³, Antoine Lucas^{1,2,4}, Pascal Haigron^{1,2}

¹ INSERM, U1099, Rennes, F-35000, France

² Université de Rennes 1, LTSI, Rennes, F-35000, France

³ Therenva, Rennes, F-35000

⁴ CIC-IT 804, Rennes, F-35000, France

⁵ ANSYS France, Villeurbanne, F-69100, France

Abstract. During the endovascular treatment of abdominal aortic aneurysm (EVAR), stiff devices are inserted into the vascular structure before stent-grafts deployment, which can lead to large deformations and so modify the preoperative sizing. In order to take into account these deformations during the intervention planning, we propose an approach which involves a FEM-based simulation to model tools-tissue interactions and a geometrical simulation to visualize stent-grafts into the estimated deformed vascular structure. The deformations have been estimated for five patients and confronted to intraoperative images. Results illustrate that the deformations of the vascular structure could be taken into account during the preoperative planning in order to better anticipate the adequacy of stent-grafts with patient anatomy.

Keywords: FEM simulation, tool/tissue interactions, geometrical simulation, intervention planning, EVAR

1 Introduction

The endovascular repair of abdominal aortic aneurysm (EVAR) has become an alternative therapy to conventional open surgery [1]. It consists in inserting a delivery system through intravascular way and deploying one or several stent-grafts at the aneurysm site in order to exclude it. This procedure has the advantage of reducing blood loss, intra-operative morbidity, and hospital stay duration.

However, EVAR shows inherent limitations that make difficult its implementation in a number of cases [2]. In particular, it requires the introduction of very stiff devices (guidewire and delivery system) which causes large deformations of the vascular structure. These endovascular tools modify the patient anatomy, in particular the length of some vascular segment as the common iliac and external iliac arteries. In clinical routine, the measures used for the stent-graft sizing are taken by analysing the undeformed preoperative CT-scan whereas stent-grafts are deployed inside a deformed vascular structure. Although these deformations are anticipated by clinical

experience, they are not objectively taken into account during the intervention planning and no dedicated tool is available to estimate them. Moreover, these deformations can lead to preoperative and intraoperative mismatching in intraoperative navigation / fusion system.

In this context, patient-specific simulation could provide a predictive tool to support intervention planning and assistance by estimating the deformation of the vascular structure. Many finite element-based studies were aimed at analyzing wall stress distribution [3], risk of rupture [4] and fluid-structure interaction [5] in abdominal aortic aneurysm. To our knowledge, only one study focused on the vascular structure deformations caused by the insertion of a stiff guidewire [6]. However, no parameters model tuning has been done in this study. The deployment of a complete aortic stent graft was also studied [7], but without taking into account the deformation caused by guidewire and delivery system insertion. Furthermore, these studies were not directly connected to endovascular intervention planning.

We propose an approach deliberately oriented towards an approximate solution consistent with the clinical workflow in order to better anticipate the adequacy of stent-grafts with patient anatomy during the intervention planning. Our method involves a FEM-based simulation to estimate, from pre-operative data, anatomical deformations due to stiff devices insertion prior to stent-graft implantation and a geometrical simulation to visualize stent-grafts into the estimated deformed vascular structure.

2 Methods

2.1 FEM-based simulation of the deformations of vascular structure

Previously, we introduced a FEM-based patient-specific simulation approach to estimate the resulting intraoperative deformations of the vascular structure due to the guidewire insertion [8]. This method was extended to estimate the deformations caused by the delivery system. The main steps of this work are summarized below.

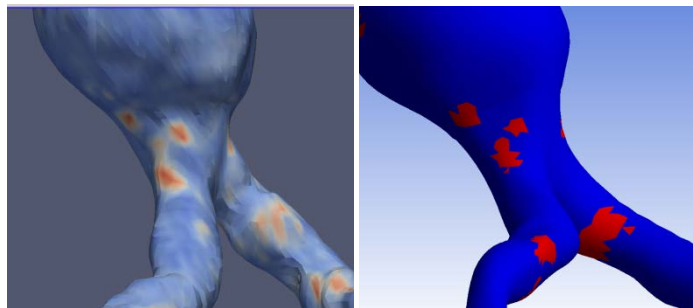


Fig. 1. High (red) and low (blue) tissue density values were obtained from preoperative CT-scan (left). The elements of the simulation mesh were then divided into two classes with different material properties (right): “calcified” (red) and “healthy” tissues (blue).

Preoperative patient data description

Pre-operative CT-scan data was analyzed with the Endosize® sizing software used in routine practice. For each patient, a complete sizing was performed according to the standards of the International Society for Vascular Surgery. The vascular structure was extracted using active contours, imported in the simulation software and then meshed using triangular shell elements. Each element was classified, through its corresponding density value obtained from the CT-scan, into two tissue categories, “healthy” and “calcified” tissues (Fig. 1). A different linear elastic material was attributed to each category (Young’s modulus: 2 MPa for “healthy” tissue and 10 MPa for “calcified” tissue).

Tool-tissue interaction model

The first simulated tool is a Lunderquist stiff guidewire (Cook®) which is inserted prior to the delivery system in order to facilitate its insertion. It was modeled by a circular beam. The second simulated tool is the delivery system whose geometry corresponds to a cylinder with a small diameter hollow core allowing the insertion of the device around the guidewire. The mechanical behavior of simulated tools was defined by linear elastic material properties derived from experimental characterization [9] (Young’s modulus and Poisson’s coefficient: 200 GPa and 0.3 for the guidewire, 668 MPa and 0.44 for the delivery system).

The boundary conditions of the model were defined with regard to anatomical knowledge. The superior extremity of the abdominal aorta and the guidewire insertion site on the femoral artery were assumed to be fixed. Additional stiffness was added between the aortic bifurcation and the internal iliac bifurcation and on the posterior side of the aorta in order to model the anatomical relationship between aorta and spine.

Simulation process

The deformed state was computed through a quasi-static simulation in order to study the final equilibrium state of the model at the end of tools insertion. The simulation consisted in initializing the guidewire into the vascular structure by positioning it on a pre-calculated path which minimizes its bending energy. The contact between the tool and the vascular structure was then activated and the guidewire was progressively relaxed until the steady state of the model is achieved. The delivery system was then displaced so that its centerline matched with the centerline of deformed guidewire. The contact between the external face of the delivery system and the internal face of the artery was then activated, and finally the delivery system was progressively relaxed until a new deformed steady state is achieved (Fig. 2).

Simulation parameters tuning

Matching of pre- and intraoperative data (fluoroscopic images) was used to evaluate simulation error and to perform parameters tuning. The geometrical transformation between the 3D preoperative coordinate system and the 2D intraoperative coordinate system was estimated using a similarity measure based on the centerlines

of the undeformed vascular structures. Registration error was calculated from the mean distance between the projected 3D preoperative centerlines and the 2D intraoperative centerlines. Simulation error was calculated from the mean distance between the centerline of the projected simulated tool and the centerline of the actually observed one. Parameters tuning was performed on a training dataset of patients. The parameters of the boundary conditions were interactively adjusted to reduce the simulation error. Behavior laws were then established between parameter values and patient data in order to obtain an adaptive model.

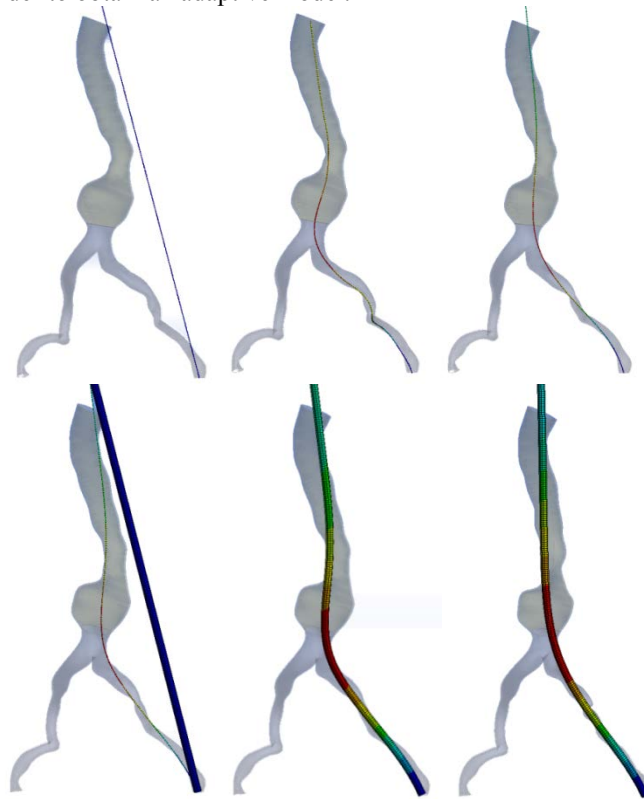


Fig. 2. Simulation of tools-tissue interactions on a patient case (guidewire on top, delivery system and guidewire on bottom)

2.2 Geometrical stent-graft placement

Mesh generation

Two stent-graft components were considered for the simulation of stent-graft placement: bifurcated main body and iliac extensions (Fig. 3). A surface mesh composed of triangular and quadrilateral elements and a centerline were used to represent stent-grafts. To represent stent-graft of different sizes, the mesh creation was parameterized by several variables (proximal and distal diameters, lengths) in order to obtain a mesh closed to the corresponding product reference. It was an automated process

which creates elements between structural contours and uses a Delaunay triangulation to mesh bifurcations.

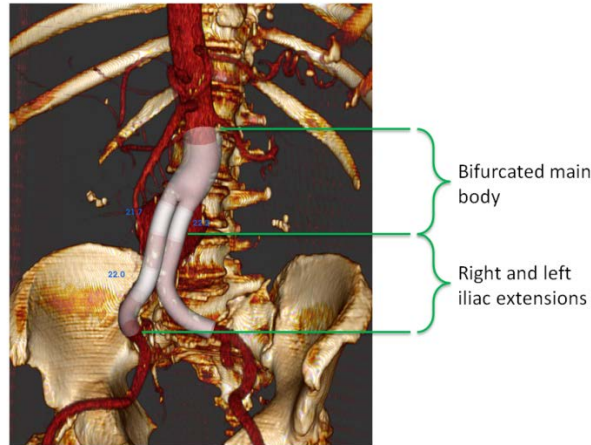


Fig. 3. Geometrical simulation of stent-grafts placement. Overlap lengths appear in blue, next to each overlap region.

Stent-graft placement

The stent-graft placement consists in positioning the stent-graft mesh on the centerline of the vascular structure. In order to compute the position of the stent-graft, the centerlines of the stent-graft and the vascular structure were oversampled with a similar point sampling. The displacements necessary to the superimposition of the two centerlines were thus calculated point to point.

Each node of the stent-graft mesh was then associated with the closest point of the stent-graft centerline. A geometrical transformation was estimated for each node in order to place the mesh around the vessel centerline (Fig. 4): the rotation was estimated using the orientation of the undeformed and deformed centerlines and the translation was estimated from the displacement of the centerline point.

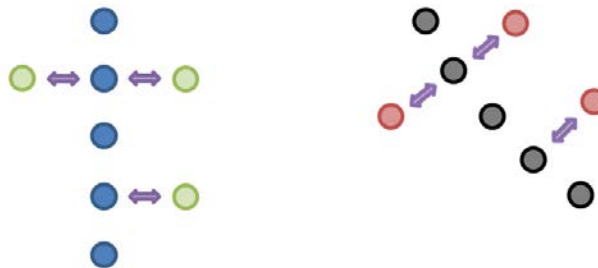


Fig. 4. Method of stent-graft positioning. Each node of the stent-graft mesh (green) was associated with a point of the stent-graft centerline (blue). The nodes (red) were then positioned around the centerline of the vascular structure (black).

Visualization

The different stent-graft meshes were restituted within a 3D reconstruction of the patient CT-scan (Fig. 3). The stent-grafts could be displayed with the original pre-operative CT-scan or with the CT-scan deformed by the guidewire and the delivery system. This deformed CT-scan was generated by interpolating and projecting the displacement field obtained by the simulation onto the CT-scan voxel grid. Each voxel of the vascular structure was then moved by the corresponding displacement. The overlap length between two consecutive stent-grafts was also calculated and displayed next to the corresponding overlap region. Each stent-graft could be moved along and rotated about the vessel centerline. After each modification, the position of the other stent-grafts was updated in order to keep the overlap length value. The insertion side could be also specified for iliac extensions.

3 Results

CT-scan data were obtained for 5 patients who underwent EVAR in the Department of vascular surgery of the University Hospital of Rennes, France. The 3D/2D registration between preoperative and intraoperative data was done for all the patients. The mean registration error was 1.5 ± 1.1 mm.

Patient	Mean	Min - Max
1	2.9 ± 1.2	0.0 - 5.2
2	3.0 ± 2.4	0.0 - 9.2
3	1.2 ± 1.1	0.0 - 8.0
4	1.7 ± 0.8	0.0 - 3.0
5	5.5 ± 3.1	0.0 - 12.3

Table 1. Error for the simulation of the resulting deformation caused by the guidewire and the delivery system (mm)

Simulations were carried out using Ansys Mechanical implicit finite element solver. The tuning of the adaptive model parameters was based on the guidewire simulation results only (mean simulation error of 2.2 ± 1.0 mm). The errors for the delivery system simulation are presented in Tab. 1. Although the parameters tuning was performed only for the guidewire simulation, the simulation of the resulting deformation caused by the guidewire and the delivery system, with a mean error of 3.0 ± 2.0 mm, gives acceptable results (Fig. 5).

Placement of stent-grafts chosen during the sizing of the 5 patients was simulated. The position of each stent-graft was adjusted in order to obtain satisfying location and sufficient overlaps. Stent-grafts position was qualitatively observed on the undeformed CT-scan and the CT-scan deformed by guidewire and delivery system. An example illustrates, in Fig. 6, the modification of the iliac extension position caused by the deformation of the vascular structure. The bottom extremity is closer to the iliac bifurcation on the deformed CT-scan than on the undeformed CT-scan. The iliac

extension placement on the CT-scan deformed by delivery device indicated that the internal iliac artery could be covered with the chosen stent-graft.

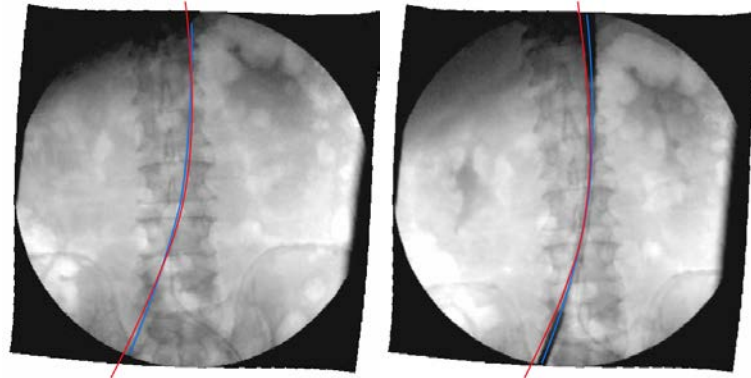


Fig. 5. Example of simulated devices projection (guidewire on left, delivery system and guidewire on right) on a patient case. Simulated devices are represented in red and the actually observed ones in blue.

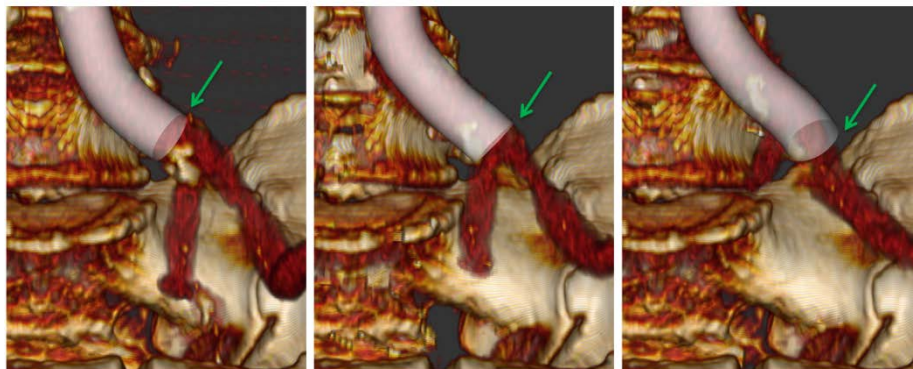


Fig. 6. Position of the bottom extremity of an iliac extension on the undeformed CT-scan (left) and the CT scan deformed by the guidewire (middle) and by the delivery system (right).

4 Conclusion

In this paper, we presented a method for the visualization of stent-grafts into deformed vascular structure, estimated by finite element simulation. Stent-grafts placement was based on a geometrical description of the different components of endovascular prosthesis. Results illustrate that the deformations of the vascular structure could be taken into account during the preoperative planning in order to better anticipate the adequacy of stent-grafts with patient anatomy.

Acknowledgements

This work was supported in part by the French national research agency (ANR) through the TecSan program (project ANGIOVISION n°ANR-09-TECS-003). This work has been partially conducted in the experimental platform TherA-Image (Rennes, France) supported by Europe FEDER.

References

- [1] Greenhalgh RM, Powell JT. “Endovascular repair of abdominal aortic aneurysm.” *N Engl J Med*, 2008;358(5):452–501.
- [2] Becquemin JP, F. Schneider, J.-B. Ricco. “Is it Time to Nail the Lid on the Coffin of Open Abdominal Aortic Aneurysm Repair? Not so Sure!” *European Journal of Vascular and Endovascular Surgery* 2012;43:625–626.
- [3] B. Doyle, A. Callanan, et T. McGloughlin, “A comparison of modelling techniques for computing wall stress in abdominal aortic aneurysms”, *BioMedical Engineering OnLine*, vol. 6, no. 1, p. 38, 2007.
- [4] B. J. Doyle, A. Callanan, M. T. Walsh, P. A. Grace, et T. M. McGloughlin, “A finite element analysis rupture index (FEARI) as an additional tool for abdominal aortic aneurysm rupture prediction”, *Vasc Dis Prev*, vol. 6, p. 114–121, 2009.
- [5] D. S. Molony, A. Callanan, E. G. Kavanagh, M. T. Walsh, et T. M. McGloughlin, “Fluid-structure interaction of a patient-specific abdominal aortic aneurysm treated with an endovascular stent-graft”. *BioMed Central*, 2009.
- [6] A. Gupta, S. Sett, et B. Wolf, “Investigation of interaction between guidewire and native vessel using finite element analysis”. *Simulia customer conference*, 2010.
- [7] S. D. Bock, F. Iannaccone, G. D. Santis, M. D. Beule, D. V. Loo, D. Devos, F. Vermassen, P. Segers, et B. Verhegghe, “Virtual evaluation of stent graft deployment: A validated modeling and simulation study”, *Journal of the Mechanical Behavior of Biomedical Materials*, vol. 13, p.129-39, 2012.
- [8] Dumenil, A.; Kaladji, A.; Castro, M.; Esneault, S.; Lucas, A.; Rochette, M.; Goksu, C.; Haigron, P., “Finite-Element-Based Matching of Pre- and Intraoperative Data for Image-Guided Endovascular Aneurysm Repair,” *IEEE Transactions on Biomedical Engineering*, vol.60, no.5, pp.1353,1362, May 2013
- [9] P. Haigron, A. Duménil, A. Kaladji, M. Rochette, B. Bou Said, S. Esneault, H. Walter-Le Berre, G. Mouktadiri, M. Castro, P. Louat, D. Roche, C. Göksu, J. Marzelle, A. Cardon, J.-P. Becquemin, A. Lucas, “Angiovision: Aortic stent-graft placement by augmented angionavigation”, *IRBM*, Volume 34, Issue 2, April 2013, Pages 167-175, ISSN 1959-0318, 10.1016/j.irbm.2013.01.016.

Augmented Reality Guidance System for Transcatheter Aortic Valve Implantation

A. Jonathan McLeod, Maria E. Currie, John T. Moore, and Terry M. Peters

Robarts Research Institute, Western University, London, Ontario, Canada
{jmcleod,mcurrie,jmoore,tpeters}@robarts.ca

Abstract. Transcatheter aortic valve implantation (TAVI) is a minimally invasive technique for performing aortic valve (AV) replacement on the beating heart. Current techniques rely on rotational angiography and/or single plane fluoroscopy for intraoperative guidance. An alternative guidance system using only transesophageal echocardiography (TEE) would be easier to integrate into the operating room and eliminate the need for nephrotoxic contrast mediums. While TEE can image the AV and assess valve function, it is not well suited for displaying the location of the TAVI catheter. A guidance system for TAVI has been developed to magnetically track and visualize the TAVI catheter in an augmented reality environment. The AV annulus and coronary ostia are delineated from TEE images acquired during rapid pacing to ensure the prosthetic valve is deployed at the appropriate location. The targeting accuracy of this system is assessed in phantom and *ex vivo* experiments.

1 Introduction

Transcatheter aortic valve implantation (TAVI) has emerged as a safe and effective treatment for aortic stenosis in patients who are not suitable for conventional surgery [6]. There have been major advancements in transcatheter valve design; however, valve deployment still relies largely on single-plane fluoroscopy, with only gross structures visible [5] and requires the use of nephrotoxic contrast medium. One approach to improving the image guidance and reducing the use of contrast agents is through the DynaCT system (Siemens AG, Erlangen, Germany). This imaging system provides intraoperative cone-beam computed tomography (CT) of the aortic root overlaid on a fluoroscopic image [3]. Intraoperative rotational angiography is performed during rapid ventricular pacing reducing the amount of contrast delivered and minimizing motion artifacts. Aortic Valve Guide software (Siemens AG, Forchheim, Germany) is used to automatically create a three-dimensional (3D) reconstruction of the aortic valve (AV) annulus, ascending aorta, cusp points, commissures, and coronary arteries [8]. Subsequently, the segmented image is superimposed on the real-time fluoroscopic image. The resulting images are used as a guidance tool during AV implantation and to select an optimal C-arm angulation for fluoroscopy. The optimal C-arm angle for TAVI deployment occurs when the nadir of all three aortic cusps are aligned, suggesting the aortic root is perpendicular to the imaging beam [4].

Previous studies have shown that use of an optimal C-arm angle for TAVI deployment is associated with decreased rates of postprocedural paravalvular leak and reduces the number of contrast enhanced images [8]. Other investigators have used intraoperative magnetic resonance imaging (MRI) to guide placement of the valve stent, resulting in successful implantation in animal studies [1]. Although this technique eliminates radiation and contrast medium exposure to the patients, such intraoperative 3D imaging is not widely available. In comparison to cone-beam CT and MRI based imaging systems, a transesophageal echocardiography (TEE) based imaging system would be more affordable, portable, and easily integrated into the operating room. Furthermore, the use of TEE does not require contrast medium or ionizing radiation. Visualization may be improved by augmenting the TEE images with virtual representations of the TAVI catheter. Such augmented reality (AR) guidance systems have previously been used for other cardiac procedures with only one so far addressing TAVI deployment [7].

The purpose of this proof of concept study was to use an AR imaging platform for TAVI placement and to evaluate the accuracy of TAVI deployment using this system. This study presents an imaging guidance system for TAVI placement to visualize both the TAVI stent and the critical aortic anatomy without exposure to contrast medium and ionizing radiation. The targeting accuracy of the system was assessed in both phantom and an *ex vivo* aortic root models. Furthermore, a digital phantom study was conducted to determine how consistently the AV annulus could be defined from TEE images.

2 Methods

2.1 Guidance System

The proposed guidance system consists of an AR environment displaying real-time ultrasound along with the location of the tracked valve stent and intraoperatively defined anatomy. Magnetic tracking sensors were integrated with the TAVI catheter and TEE probe, allowing geometric models of these tools to be displayed at their corresponding positions in the AR environment. The phantom and *ex vivo* studies were performed using the Philips Sonos 7500 (Philips Healthcare, Andover, MA) with a six degree of freedom sensor was attached to the TEE probe and a second similar sensor was affixed to the rigid portion of the TAVI catheter tip. The tracked TEE probe was calibrated using a Z-bar phantom. Once the valve was crimped onto the catheter, a quick calibration was performed using a custom-built tracked calibration block designed to hold the catheter shaft and valve in a precise configuration (Figure 1). This allowed the crimped prosthetic valve to be magnetically tracked.

For TAVI deployment, visualization of the AV annulus and coronary arteries is required in order to safely complete the tool guidance task. These features can be identified using tracked ultrasound image data. Three points defining each commissure of the AV are identified on the valve annulus. These points define the valve plane and are displayed to the user along with a tubular spline outlining the valve (Figure 1). When visible in the echo image, the coronary ostia can also

be delineated by the user and displayed in the guidance system. Virtual models of the tracked TAVI catheter and TEE probe with an ultrasound fan showing live video can be displayed relative to the preoperatively defined anatomy. A target plane is then created at a user defined distance from the commissures chosen based on the profile of the valve.

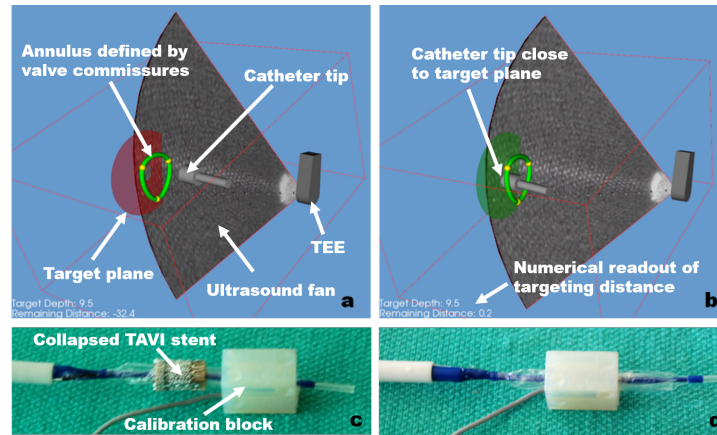


Fig. 1. AR guidance (a) system components and (b) valve approaching the target. TAVI stent and calibration block (c) and calibration procedure (d)

2.2 Surgical Workflow

The standard of care for performing this procedure under fluoroscopic guidance employs rapid ventricular pacing to effectively arrest the motion of the valve during the procedure. Rapid pacing is performed twice during the procedure. First, to test the leads prior to advancing the catheter into the AV and then again to arrest cardiac motion as the valve is deployed. Our AR guidance system is designed to assist the surgeon with establishing the correct location for deployment of the TAVI valve without fluoroscopy. To achieve this, prior to advancing the valve catheter, the echocardiographer identifies the three AV commissures to define the AV annulus. The first rapid pacing provides an ideal opportunity for acquiring these images as the heart is static and in the same condition it will be in during final deployment of the valve, obviating the need for complex valve tracking algorithms. Next, the surgeon determines the appropriate target depth relative to the AV annulus for the TAVI valve. By overlaying the geometric models on the real ultrasound image data, the surgeon is able to assess the accuracy of these representations in real-time. If the features have moved, they can be redefined before proceeding.

The technology associated with the AR guidance system can be easily integrated into the operating room. The NDI AuroraTM Tabletop magnetic field

generator is specifically designed to work in the presence of ferrous and conducting objects. It has a large field of view and easily fits on top of the OR table. Sensors attached to the TEE probe and surgical tools should not impede normal OR workflow. The proposed system has a smaller footprint and requires less equipment than current techniques requiring fluoroscopy. Furthermore, the cost associated with this technology is much less than alternatives such as intraoperative MRI or cone beam CT.

2.3 Phantom Study

A phantom study was the first step in validating the AR guidance system. In this study, the targeting accuracy of the guidance system was assessed in a phantom where the aorta was modeled by a transparent plastic tube with an inner diameter of 23.5mm. The proximal end of the tube was clearly visible in ultrasound and was used to model the AV annulus. Three points were defined on the TEE image of the phantom to define the aortic valve plane. Using the guidance system, the valve was deployed at a specified depth beyond the aortic valve plane. A depth of 9.5mm was chosen as the target depth for these experiments. Once deployed, the residual error reported by the guidance system was recorded and the actual depth of deployment was measured against a ruler attached to the side of the phantom. Finally, the difference between the actual depth and that recorded by the guidance system was also reported. This experiment was repeated 8 times with a single operator controlling the catheter. (Figure 2).

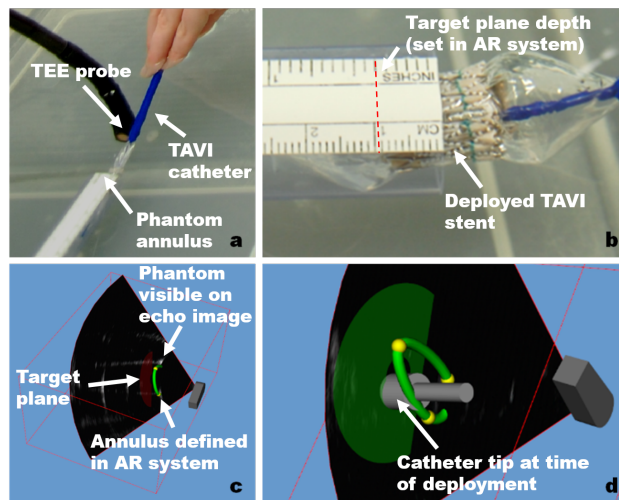


Fig. 2. (a) Experimental setup of the phantom as the catheter is being advanced. (b) Prosthetic valve after deployment with the depth visible on the ruler. (c) Guidance system with the tube visible on the TEE image. (d) Guidance system at time of the deployment shown in b.

2.4 Annulus Localization

The previous experiment assessed the targeting accuracy of the system in a controlled environment where the annulus was clearly visible and well defined in the TEE images. *In vivo*, defining the valve annulus is more challenging. It is essential that the landmarks used to delineate the valve annulus be well defined with minimal variability in identifying these landmarks. Since the commissures of the AV are stationary hinge points visible in echocardiography, the guidance system may use these points to define the AV annulus. To assess the interoperator variability in identifying these landmarks, four subjects identified the three commissures along the AV annulus in five full volume TEE images of the aortic root in diastole. These images are consistent with standard intraoperative imaging and provided a view similar to that of rapid pacing.

2.5 Proof of Concept *Ex Vivo* Study

The next step in validating this AR guidance system was an *ex vivo* study on a porcine heart. The operator was asked to deploy the TAVI valve at a target distance from the annulus based on the profile of the valve. After deployment, the location of the proximal struts was demarked on the inner surface of the aorta with a suture. Following collapsing and removing the stent valve, the actual distance from the proximal valve struts on the ventricular side to the annulus was measured using calipers (Figure 3).



Fig. 3. (a) Setup for the *ex vivo* experiment to simulate a mid esophageal view. (b) Dissected specimen after valve deployments.

3 Results

The signed deployment errors from the phantom deployment studies are reported in Table 1 with positive errors indicating the valve was deployed posterior to the desired location. The errors reported by the guidance system were very low, all less than 0.4 mm from the desired deployment location. Since the guidance system was the only feedback used in deciding where to deploy the valve, it is

expected that these errors be minimal. The actual error measured from the tip of the deployed valve prosthesis to the desired deployment location ranged from -1.7 to 2.6 mm. The mean absolute actual error was 1.2 mm (SD 1.0). The overall distance error calculated from the difference between the distance reported by the guidance system and the actual measured distance ranged from -2.0 to 3.0 mm. The mean overall distance error was 1.3 mm (SD 1.1). The variation in

Table 1. Error in Deployment of TAVI Stent in Phantom

	Trial	1	2	3	4	5	6	7	8
Guidance (mm)	0.0	0.3	0.1	0.1	0.4	-0.1	-0.4	0.1	
Actual (mm)	-0.7	-1.7	-0.2	2.3	0.1	-0.7	2.6	0.3	
Difference (mm)	-0.7	-2.0	-0.3	2.2	-0.3	-0.6	3.0	0.1	

localizing the valve commissures is reported in Table 2. The average standard deviation of the position of the three commissures was recorded for each volume. The standard deviation in the direction perpendicular to the aortic annular plane was also calculated. The variation in identifying the commissures was quite low, especially in the out-of-plane direction, indicating consistent identification of the commissures between subjects. The errors for the two deployments are reported

Table 2. Interoperator Variability in Localizing Valve Commissures

Volume Number	1	2	3	4	5	Mean
Total (mm)	1.1	3.8	1.6	2.3	1.1	2.0
Out-of-Plane (mm)	0.7	2.3	0.5	0.6	0.3	0.9

in Table 3 with overall errors of 6.3 mm and 1.5 mm. As the commissures were not visible in the single plane echocardiography of the static AV, the nadir points were used instead.

Table 3. Error in Deployment of TAVI in *Ex Vivo* Study

	Trial	1	2
Guidance (mm)	0.0	-0.5	
Actual (mm)	6.3	1.0	
Difference (mm)	6.3	1.5	

4 Discussion

This study presents an imaging guidance system for TAVI placement to visualize both the TAVI stent and the critical aortic anatomy without exposure to contrast medium and ionizing radiation. Comparing the results obtained in this study with existing techniques is challenging. In fluoroscopy studies, the error in deployment is not reported as the accuracy of deployment is generally determined by the visual inspection of the radiopaque valve. Nevertheless, new fluoroscopy based image guidance systems augment the real-time fluoroscopy with overlays showing the 3D aortic root structure obtained from CT. These studies measure the error in overlay between their own model and real time fluoroscopy. While not the same as a true targeting error, these studies provide a baseline for clinically acceptable errors. For example, the error in overlay of DynaCT on real-time fluoroscopy has been reported between $1.9\pm 1.5\text{mm}$ and $3.9\pm 3.1\text{mm}$ [2,9]. Generally, errors in positioning less than 5mm are acceptable.

In the phantom study, the errors reported by the guidance system were very low, all less than 0.4mm from the desired deployment location indicating that the subject was able to successfully follow the guidance system and deployed the valve at the indicated depth. The overall distance error was 1.3mm (SD 1.1) indicating that good valve positioning could be achieved using the AR system.

The digital phantom study was conducted to determine how consistently the AV annulus could be defined using commissures from full volume TEE images. The standard deviation of the identified commissure was 2.0mm in 3D and 0.9mm in the out-of-plane direction. The good localization of the fiducials in the out-of-plane direction indicates these landmarks are suitable for defining the valve plane.

When the deployment experiment was repeated in an *ex vivo* aortic root, the overall distance error increased to 6.3 and 1.5mm in the two trials. This disparity can be accounted for by the operator's difficulty in identifying the AV annulus. While the valve commissures were easily identifiable in static volumetric images of a human patient, these structures were not visible using single plane echocardiography of *ex vivo* porcine tissue. Instead, the valve nadir were used to define the valve annulus but there was considerable uncertainty in locating these points. It should be noted that the distance from the nadir to the commissures was approximately 8mm and all points between the nadir and commissures where the cusps attached to the aortic wall had similar appearance in single plane echocardiography. Both trials overshot the nadir plane, consistent with misidentifying points along the cusp attachments as nadir points. This study will be repeated with a matrix array TEE capable of volumetric and bi-plane imaging which will improve annular localization and is consistent with modern intraoperative echocardiography.

5 Conclusion

This study presents the feasibility of an image guidance system for TAVI placement to visualize both the TAVI stent and the critical aortic anatomy without

exposure to contrast medium and ionizing radiation. The phantom studies indicated that in a well-defined annulus targeting errors on the order of 1mm were achievable. The localization of accuracy of the commissures in the digital phantom experiment was also on the order of 1mm. This suggests an accurate guidance system is realizable using the commissures to define the valve plane. The errors in the two *ex vivo* trials of 6.3 and 1.5mm were higher than the phantom results but were consistent with the inability to localize specific points along the leaflet cusps' attachments to the aortic wall. This study will be repeated with a matrix array transducer so that volumetric and biplane images can be used.

Acknowledgments This work was supported by NSERC, CIHR, and CFI. Graduate student funding for Jonathan McLeod was provided by OGS. The authors would also like to thank Dr. David McCarty, Martin Rajchl and Feng Li for providing the clinical images used in the annulus localization study.

References

1. Horvath, K.A., Mazilu, D., Guttman, M., Zetts, A., Hunt, T., Li, M.: Midterm results of transapical aortic valve replacement via real-time magnetic resonance imaging guidance. *J Thorac Cardiovasc Surg* 139(2), 424–430 (2010)
2. Kempfert, J., Rastan, A., Noettling, A., John, M., van Linden, A., Blumenstein, J., Linke, A., Schuler, G., Mohr, F.W., Walther, T.: Perioperative dynact for improved imaging during transapical aortic valve implantation. In: *Circulation*. vol. 122 (2010)
3. Kempfert, J., Falk, V., Schuler, G., Linke, A., Merk, D., Mohr, F.W., Walther, T.: Dynact during minimally invasive off-pump transapical aortic valve implantation. *Ann Thorac Surg* 88(6), 2041 (2009)
4. Kempfert, J., Noettling, A., John, M., Rastan, A., Mohr, F.W., Walther, T.: Automatically segmented dynact enhanced imaging during transcatheter aortic valve implantation. *Journal Am Coll Cardio* 58(25), e211 (2011)
5. Lang, P., Peters, T.M., Kiaii, B., Chu, M.W.: The critical role of imaging navigation and guidance in transcatheter aortic valve implantation. *J Thorac Cardiovasc Surg* 143(6), 1241–1243 (2012)
6. Leon, M.B., Smith, C.R., Mack, M., Miller, D.C., Moses, J.W., Svensson, L.G., Tuzcu, E.M., Webb, J.G., Fontana, G.P., Makkar, R.R., et al.: Transcatheter aortic-valve implantation for aortic stenosis in patients who cannot undergo surgery. *New Engl J Med* 363(17), 1597–1607 (2010)
7. Luo, Z., Cai, J., Gu, L.: A pilot study on magnetic navigation for transcatheter aortic valve implantation using dynamic aortic model and us image guidance. *International journal of computer assisted radiology and surgery* pp. 1–14 (2013)
8. Poon, K.K., Crowhurst, J., James, C., Campbell, D., Roper, D., Chan, J., Incani, A., Clarke, A., Tesar, P., Aroney, C.: Impact of optimising fluoroscopic implant angles on paravalvular regurgitation in transcatheter aortic valve replacements-utility of three-dimensional rotational angiography. *EuroIntervention* 8(5), 538 (2012)
9. Zheng, Y., John, M., Liao, R., Nottling, A., Boese, J., Kempfert, J., Walther, T., Brockmann, G., Comaniciu, D.: Automatic aorta segmentation and valve landmark detection in c-arm ct for transcatheter aortic valve implantation. *IEEE TMI* 31(12), 2307–2321 (2012)

Automatic Flow Diverter Detection in Cerebral C-arm CT Images

Ying Zhu

Siemens Corporation, Corporate Technology
Princeton New Jersey, USA
(yingzhu@siemens.com)

Abstract. We propose a method of automatic detection and segmentation of flow diverters from cerebral C-arm CT images. A probabilistic framework based on a joint appearance and shape model is developed to locate and trace flow diverters in volumetric data. The proposed method provides a solution to automating the workflow of intracranial aneurysm treatment and assessment of flow diverter placement through post-operative scans.

1 Introduction

Endovascular stenting is a widely used procedure to treat intracranial aneurysms. Flow-diverter stents such as the Pipeline stent and the Silk stent (Fig. 1 (a)) have been developed in recent years. They form high-coverage mesh once expanded and thus offer the potential of aneurysm occlusion related to flow disruption [4]. Treatment with flow diverters is promising especially for aneurysms of unfavorable morphological features such as wide neck, large size, fusiform morphology, etc [5] and is gaining widespread acceptance [6]. In this work, we address the issue of automating the workflow of intracranial aneurysm treatment and the assessment of flow diverter placement through post-operative scans.

Following a procedure of flow diverter placement, a post-operative C-arm CT scan is acquired for clinicians to visually assess the outcome of the procedure. As Fig. 1(b) shows, a flow diverter, as a relatively small device, is difficult to locate inside brain tissues. A clinician has to manually adjust visualization to locate the flow diverter and make it more visible for clinical evaluation. In some cases, further manual segmentation is performed to separate the flow diverter from surrounding image content for quantitative evaluation. Fig. 1(c) shows a close-up view of the flow diverter in Fig. 1(b) after manual adjustment of the visualization. To obtain quantitative measurements of flow diverter placement such as its diameter and length, manual segmentation may be required to separate the flow diverter from its surroundings. To eliminate the need of manual adjustment which is difficult and time consuming, we propose a method of automatic detection and segmentation of flow diverters using both image appearance and object shape information. The proposed technique enables further quantitative analysis and measurement of flow diverter placement.

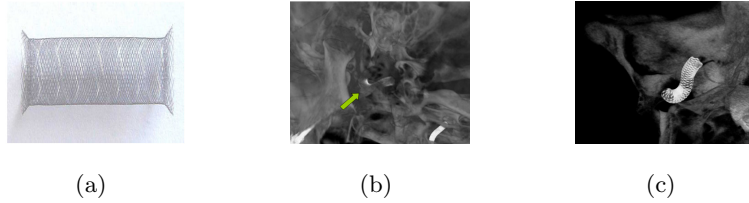


Fig. 1. Flow diverter image. (a) Silk stent [11]. (b) Visualization before manual adjustment with an arrow pointing to the flow diverter. (c) Visualization after manual adjustment of window center and window width and zooming.

Though automatic detection and segmentation of flow diverters in post-operative brain images is a relatively new research topic, several techniques have been developed for segmentation and registration of stent grafts. In [1], Klein et al. proposed a graph-based method to automatically segment stent grafts and obtain a geometric stent model from CT data. In [2], Langs et al. presented a learning framework to segment endograft wires and estimate their shape deformation from cardiac gated CT sequences. In [3], Demirci et al. described a registration framework to automatically match a 3D model of the stent graft to an intraoperative 2D image showing the device. Our method focuses on automatically identifying a flow diverter and estimating its tubular shape model for optimal visualization.

2 Method

An expanded flow diverter is seen as a convoluted tubular object in a C-arm CT image. Our goal is to automatically detect, locate and extract the flow diverter from a volumetric data. As shown in Fig. 1(c)(d) where an 2D multi-planar rendering (MPR) view of two cerebral images with flow diverters in the central regions is displayed, it is relatively easy to separate a flow diverter from brain tissues due to the difference in their intensity values, but there is considerable similarity between flow diverters and bony structures in terms of the intensity levels and the local image appearance. In addition, the radii and length of the expanded flow diverters vary in different cases, and so does the image resolution.

To deal with these challenges, we have developed a learning-based approach which forms a joint appearance and shape model for flow diverter detection and shape estimation in volumetric images. The method consists of two key elements, a learning-based appearance model and a three-dimensional tubular shape model. Fig. 2 illustrates the major steps of the proposed method. First, an orientation invariance appearance detector is used to determine the potential locations of a flow diverter. By analyzing the probability map of the appearance detector, we generate multiple hypotheses of flow diverter locations. Then a Bayesian framework is applied to examine each hypothesis, where a tubular shape model and a cross section appearance model are used to trace the flow

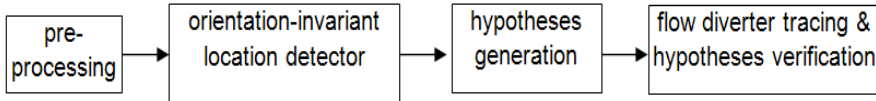


Fig. 2. Diagram of flow diverter detection.

diverter and verify the hypothesis. The techniques involved are presented in the following discussions.

2.1 Orientation invariant appearance-based segment detector

A flow diverter may appear at an arbitrary location and orientation in a volumetric image. The first step of the proposed method is to determine the location information. An appearance-based flow diverter segment detector is learned from flow diverter images to perform the task.

As Fig. 3(a) shows, two sets of training samples are generated from annotated flow diverter images where the ground truth of the flow diverter centerline and radii has been obtained through manual annotation. A positive sample ($I, l = 1$) is defined as a local box (i.e subvolume) I placed on a centerline point of a flow diverter and containing a short segment of the flow diverter. The size of the box is proportional to the local radius of the flow diverter segment. A negative sample ($I, l = -1$) is defined as a local box I with a fixed size placed in regions that do not contain flow diverters but have high intensity values and strong image gradients such as edges of bones. We then use the Adaboost algorithm [7] to learn a binary classifier that separates segments of flow diverters from other image structures. In practice, many other classification algorithms can be used as well. To make the appearance detector invariant to the local orientation of flow diverters, the set of positive training samples is constructed to include flow diverter segments from uniformly distributed orientations. From each local segment of annotated flow diverters, we generate multiple training samples by assigning the segment a set of synthesized orientations uniformly sampled in the three-dimensional sphere. Steerable features [9] calculated from local image gradients, intensity and symmetry around the centerline point are used to learn weak hypotheses $\{h_j(I)\}$. The scale of the steerable features is proportional to the size of the local segment. The number of steerable features remains the same for all training samples. Adaboost learns a strong hypothesis by combining multiple weak hypotheses, $f(I) = \sum_j \alpha h_j(I)$. The posterior probability of a local subvolume I belonging to the positive class, i.e. containing a flow diverter segment, can be formulated as [8]

$$P_{seg}(l = 1|I) = \frac{e^{f(I)}}{e^{f(I)} + e^{-f(I)}} \quad (1)$$

To determine the location of a flow diverter, we scan through the entire volume and calculate the posterior probability of the segment detector for all voxel

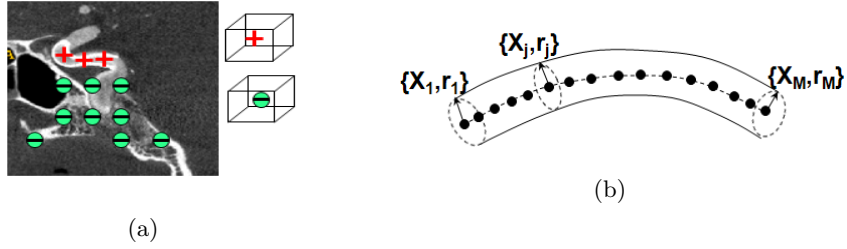


Fig. 3. (a) Training samples for flow diverter segment detector. (b) Curved tube model.

locations. A 3D probability map is hence produced by the appearance-based detector. The value at a location indicates the probability that a flow diverter appears and is centered at that location (Fig. 5(b)). Since flow diverters appear in high intensity levels, to reduce the computation, a pre-processing step can be introduced in practice to quickly rule out homogeneous image regions with low intensity values and set their probability to a low value instead of computing the classifier response exhaustively.

2.2 Joint appearance and shape model

The appearance-based segment detector provides orientation invariant location information, where points on a flow diverter’s centerline tend to have high probability values. To further estimate the orientation and shape information of the flow diverter, a probabilistic framework incorporating a joint appearance and shape model is adopted. The 3D shape of an expanded flow diverter can be modeled as a curved tube and represented by a centerline curve and the associated radii shown in Fig. 3(b). Consider a parametric representation $\{\mathbf{x}(t, \Theta), r(t, \Theta)\}$, where $\mathbf{x}(t, \Theta)$ and $r(t, \Theta)$ represent respectively the centerline curve and the corresponding radius with parameter Θ . An example representation is the parametric spline, where Θ comprises a set of control points. Without loss of generality, we can represent the tube by a set of discrete centerline points and the corresponding radii $\{\mathbf{x}_k = \mathbf{x}(t_k), r_k = r(t_k) : k = 1, \dots, M\}$ (Fig. 3(b)). Denote $\mathbf{x}_{1:M} = \{\mathbf{x}_1, \dots, \mathbf{x}_M\}$ and $r_{1:M} = \{r_1, \dots, r_M\}$. Our problem becomes to estimate the parameters $\{\mathbf{x}_{1:M}, r_{1:M}\}$ from a given image. Note that the parametric tube representation $\{\mathbf{x}(t, \Theta), r(t, \Theta)\}$ can easily be derived from $\{\mathbf{x}_{1:M}, r_{1:M}\}$ through spline interpolation. The Bayesian formulation of the problem is written as

$$p(\mathbf{x}_{1:j}, r_{1:j} | I) \propto p(\mathbf{x}_{1:j-1}, r_{1:j-1} | I) p_S(\mathbf{x}_j, r_j | \mathbf{x}_{1:j-1}, r_{1:j-1}) p_A(I | \mathbf{x}_{1:j}, r_{1:j}) \quad (2)$$

where $p_S(\mathbf{x}_j, r_j | \mathbf{x}_{1:j-1}, r_{1:j-1})$ defines a shape model as the conditional probability distribution of the location of a centerline point \mathbf{x} and the corresponding radius r_j given the location of all the preceding points and the associated radii. $p_A(I | \mathbf{x}_{1:j}, r_{1:j})$ defines a local appearance model as the likelihood of local image appearance at a given centerline point $\{\mathbf{x}_j, r_j\}$.

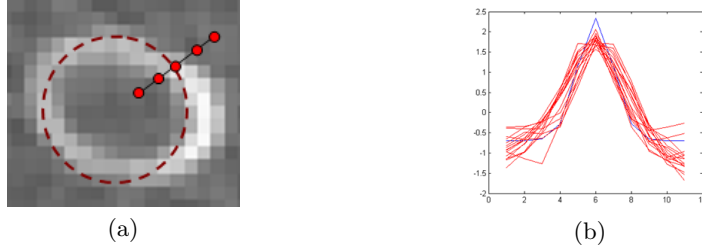


Fig. 4. Local appearance model. (a) Flow diverter cross section image and radial profile samples. (b) Intensity profiles in 16 radial directions (shown in red) and the corresponding match filter (shown in blue).

Assume that a set of centerline points $\{\mathbf{x}_1, \dots, \mathbf{x}_{j-1}\}$ and associated radii $\{r_1, \dots, r_{j-1}\}$ have been identified. A smooth centerline curve $\mathbf{x}(t)$ and a radius function $r(t)$ can be obtained through spline interpolation. If we assume C^1 continuity of $\mathbf{x}(t)$, the location of the next centerline point \mathbf{x}_j can be predicted from the tangent $\mathbf{x}'(t = t_{j-1}) \approx (\mathbf{x}_{j-1} - \mathbf{x}_{j-2}) / (t_{j-1} - t_{j-2})$ as $\hat{\mathbf{x}}_j = \mathbf{x}_{j-1} + \mathbf{x}'(t_{j-1})(t_j - t_{j-1})$. We formulate the shape model p_S as

$$p_S(\mathbf{x}_j, r_j | \mathbf{x}_{1:j-1}, r_{1:j-1}) = \mathcal{G}(\mathbf{x}_j; \mathbf{x}_{j-1} + \mathbf{x}'(t_{j-1})(t_j - t_{j-1}), \sigma_{\mathbf{x}}^2 I) \cdot \mathcal{G}(r_j; r_{j-1}, \sigma_r^2) \quad (3)$$

where $\mathcal{G}(z; z_0, \Sigma)$ denotes a Gaussian distribution with mean z_0 and covariance Σ . The shape model imposes a smoothness constraint on the centerline and radius of the curved tube. The model parameters $\{\sigma_{\mathbf{x}}^2, \sigma_r^2\}$ can be estimated from the ground truth $\{\mathbf{x}_j, r_j\}$ of flow diverter examples by fitting Gaussian models to the ground truth data.

The local appearance model p_A is defined on the intensity profiles from the cross section image of the flow diverter. As Fig. 4(a) shows, a cross section image is generated from a local 2D plane orthogonal to the centerline curve. The local stent strut appears as a bright ring in the cross section image. To model the local image appearance, we sample intensity profiles along multiple radial directions. Fig. 4(b) shows the normalized intensity profiles in 16 radial directions. Denote the normalized intensity profile sampled in the i -th radial direction as $I_{p,i}(\mathbf{x}_j, \mathbf{x}'_j, r_j) = [I_{p,i,-n}(\mathbf{x}_j, \mathbf{x}'_j, r_j), \dots, I_{p,i,0}(\mathbf{x}_j, \mathbf{x}'_j, r_j), \dots, I_{p,i,n}(\mathbf{x}_j, \mathbf{x}'_j, r_j)]$ ($i = 1, \dots, n$). A symmetric match filter $f_p = [f_{p,-n}, \dots, f_{p,0}, \dots, f_{p,n}]$ is defined by an exponential function $f_{p,k} = ce^{-\gamma k^2}$, where c is a normalizing factor and γ is estimated from the ground truth intensities. The local appearance model is defined as

$$p_A(I | \mathbf{x}_{1:j}, r_{1:j}) = p_A(I | \mathbf{x}_j, \mathbf{x}'_j, r_j) = \prod_{i=1}^n \mathcal{G}(I_{p,i}(\mathbf{x}_j, \mathbf{x}'_j, r_j); f_p, \sigma_A^2 I) \quad (4)$$

The intensity profile is modeled as a Gaussian distribution with mean f_p and covariance σ_A^2 estimated from the data.

2.3 Flow diverter detection

Flow diverter detection is implemented as hypothesis generation followed by hypothesis verification. As Fig. 5(b) shows, the 3D probability map generated by the flow diverter segment detector is first smoothed, and the local maxima in the smoothed probability map are located. These local maxima are used as seed points to establish hypotheses of flow diverter centerlines. Starting from each located seed point, the hypothesis validation step traces a flow diverter centerline and associated local radii using the joint appearance and shape model (2). The detection algorithm is summarized as follow:

- Smooth the 3D probability map with a low-pass Gaussian filter; detect local maxima $\{\mathbf{z}_k\}$ in the smoothed probability map (Fig. 5(b));
- At each local maximum point \mathbf{z}_k , establish a centerline hypothesis by setting $\mathbf{x}_1 = \mathbf{z}_k$, and compute the maximum likelihood (ML) estimate of the tangent direction \mathbf{x}'_1 and radius r_1 using the local appearance model (4)

$$\{\hat{\mathbf{x}}'_1, \hat{r}_1\} = \underset{\mathbf{x}'_1, r_1}{\operatorname{argmax}} p_A(I|\mathbf{x}_1, \mathbf{x}'_1, r_1) \quad (5)$$

- Trace the centerline in the tangent direction by iteratively computing the ML estimate of the next centerline point \mathbf{x}_j and radius r_j for $(j = 2, 3, \dots)$ using the joint appearance and shape model (2)

$$\{\hat{\mathbf{x}}_j, \hat{r}_j\} = \underset{\mathbf{x}_j, r_j}{\operatorname{argmax}} p_S(\mathbf{x}_j, r_j | \mathbf{x}_{1:j-1}, r_{1:j-1}) p_A(I|\mathbf{x}_j, \mathbf{x}'_j, r_j) \quad (6)$$

- Stop tracing if the likelihood of the appearance model $p_A(I|\mathbf{x}_j, \mathbf{x}'_j, r_j)$ falls below a pre-determined threshold;
- Repeat centerline tracing in the opposite direction, and connect two sets of traced centerline points at \mathbf{x}_1 ;
- If multiple hypotheses are detected, the likelihood defined in (2) is compared with a pre-determined threshold to accept or reject hypotheses.

Fig. 5 shows the intermediate results of hypothesis generation and verification.

3 Results

The proposed method was tested on 9 clinical datasets each containing a flow diverter. The image resolution varies between $0.088mm$ and $0.216mm$. The radii of flow diverter vary between $1.57mm$ and $2.15mm$ from manual annotation. The appearance detector was learned from a total of 56180 positive samples and 195303 negative samples with image resolution of $0.5mm$. A test image was first resampled to the fixed resolution $0.5mm$ before flow diverter detection was applied. Out of 9 datasets, flow diverters were correctly detected in 8 cases where the entire flow diverter was detected and completely traced. Flow diverter was detected and only partially traced in 1 case. The results are shown in Fig. 6.

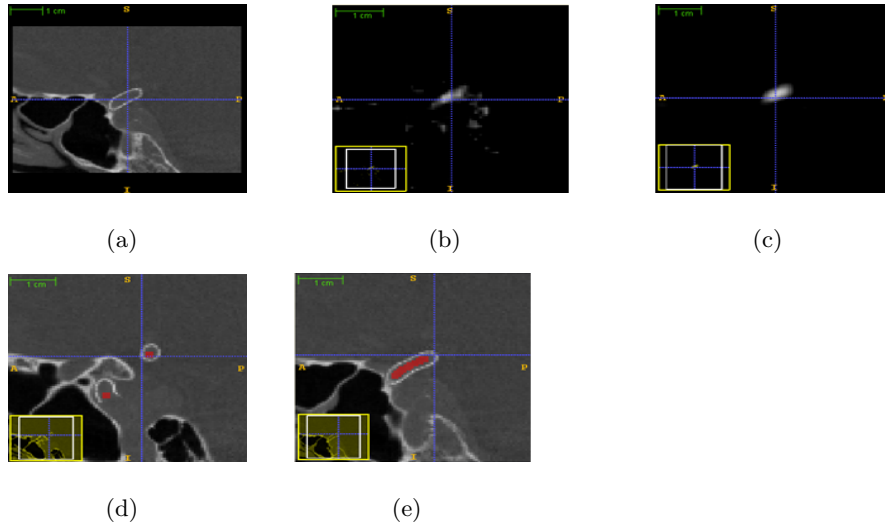


Fig. 5. Flow diverter detection. (a) Input volume. (b) Probability map. (c) Smoothed probability map. (d) Seed points displayed on input image (shown in red). (e) Traced centerline points (shown in red).

4 Conclusions

We have presented a probabilistic framework for automatic detection and segmentation of expanded flow diverters in cerebral C-arm CT images. A joint appearance and shape model is used to fuse the information of flow diverter shape and local appearance information obtained by learning. Promising results have been shown on several clinical data. The proposed method can bring clinical benefits by automating the post-operative workflow and providing quantitative measurements to assess flow diverter placement. Our future work is to improve the accuracy of the shape estimation and extend the method to other types of stent devices. In addition, quantitative evaluation will be performed to compare the results produced by the automatic algorithm against manual annotation.

References

1. A. Klein, J.A. van der Vliet, L.J. Oostveen, Y. Hoogeveen, L.J. Kool, W.K. Renema and C.H. Slump, Automatic Segmentation of The Wire Frame of Stent Grafts from CT data., *Medical Image Analysis*, 16(1):127-39, 2012.
2. G. Langs, N. Paragios, P. Desgranges, A. Rahmouni and H. Kobeiter, Learning deformation and structure simultaneously: In situ endograft deformation analysis, *Medical Image Analysis*, 15(1):12-21, 2011.
3. S. Demirci, A. Bigdelou, L. Wang, C. Wachinger, M. Baust, R. Tibrewal, R. Ghotbi, H-H. Eckstein and N. Navab, 3D Stent Recovery from One X-ray Projection, *MIC-CAI*, pp. 178-185, 2011.

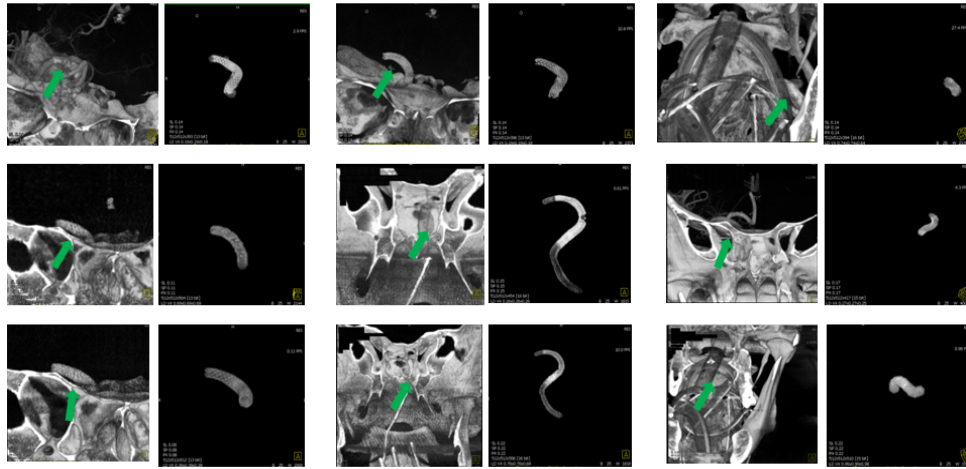


Fig. 6. Results of flow diverter detection (Left image: original volume with an arrow pointing to the location of the flow diverter; Right image: detected and segmented flow diverter.)

4. B. Lubicz, L. Collignon, G. Raphaeli, J. Pruvo, M. Bruneau, O. De Witte, X. Leclerc, Flow-Diverter Stent for the Endovascular Treatment of Intracranial Aneurysms A Prospective Study in 29 Patients With 34 Aneurysms, *Stroke*, pp. 2247-2253, 2010.
5. S. Yu, C. Kwok, P. Cheng, K. Chan, S. Lau, W. Lui, K. Leung, R. Lee, H. Cheng, Y. Cheung, M. Chan, G. Wong, J. Hui, Y. Wong, C. Tan, W. Poon, K. Pang, A. Wong, K. Fung, Intracranial Aneurysms: Midterm Outcome of Pipeline Embolization device—A Prospective Study In 143 Patients With 178 Aneurysms, *Radiology*, 265(3):893-901, 2012.
6. J. Raymond J, F. Guilbert, and A. Weill, S. Georganos, L. Juravsky, A. Lambert, J. Lamoureux, M. Chagnon, D. Roy, Long-term Angiographic Recurrences After Selective Endovascular Treatment of Aneurysms with Detachable Coils. *Stroke*, 34:1398-403, 2003.
7. R. E. Schapire, Y. Singer, Improved Boosting Algorithms Using Confidence-rated Predictions, *Machine Learning*, pp. 80-91, 1999.
8. J. Friedman, T. Hastie, R. Tibshirani, Additive Logistic Regression: a Statistical View of Boosting, *Annals of Statistics*, 28(2):337-407, 2000.
9. G. Gonzale, F.Aguet, F.Fleure, M. Unser, P. Fua, Steerable features for statistical 3D dendrite detection, *MICCAI*, pp.625-632, 2009.
10. H. V. Poor, *An Introduction to Signal Detection and Estimation*, Springer, 1994.
11. <http://www.mhra.gov.uk/Publications/Safetywarnings/MedicalDeviceAlerts/CON076289>.

Investigation of Hemodynamics in a Large Unruptured Intracranial Aneurysm Using Computational Fluid Dynamics Technique

Wen Liu¹, Lin Shi¹, Tianfu Wang², Defeng Wang^{1,3,*}, Simon C.H. Yu^{1,**}

¹Department of Imaging and Interventional Radiology, The Chinese University of Hong Kong, Hong Kong SAR, P.R. China

²Shenzhen Key Laboratory of Biomedical Engineering, School of Medicine, Shenzhen University, Shenzhen, P.R. China

³CUHK Shenzhen Research Institute, Shenzhen, P.R. China
{dfwang, simonyu}@cuhk.edu.hk

Abstract. Blood flow dynamics are thought to play a crucial role in the progression, growth and rupture of intracranial aneurysms. The hemodynamic variations in the aneurysm are often assumed to be related with its continuous growth and eventual rupture. In addition, the assessment of blood flow pattern in the aneurysm is important for the correct placement of intravascular stents or embolization coils, especially for the effective treatment of large aneurysm. The purpose of this research is to investigate the hemodynamics in a large unruptured intracranial aneurysm using computational fluid dynamic (CFD) technique. In particular, CFD is conducted to analyze the effects of parent artery segmentation on intra-aneurysmal hemodynamics. The sensitivity of blood flow pattern is also assessed with respect to the inflow velocities. Finally, we visualize and compare the intra-aneurysmal flow pattern, total pressure and wall shear stress in different conditions.

1 Introduction

Hemodynamics is identified as a fundamental factor in the mechanisms of aneurysm progression, growth and rupture. An accurate understanding of the mechanisms plays

an important role in rupture risk assessment and aneurysm treatment [1]. Investigation of intracranial aneurysm hemodynamics has attracted increasing attention during the past decade. Yu et al. [1] have conducted an Asia's first clinical research on the utilization of pipeline embolization device in treating intracranial aneurysms (ICAs). However, a minority of patients still failed to recover fully in the postoperative follow-up. This motivates us to investigate the hemodynamics in unruptured ICAs using the computational fluid dynamics (CFD) technique before operation.

In addition, the aneurysm rupture is a cause of subarachnoid hemorrhage with high mortality and morbidity rates. The risk of rupture increases directly with aneurysm size. Thus more attention is now being paid to the investigation of hemodynamics in large unruptured aneurysms [2,3]. According to current literature, remarkable achievements have been made in recent years. From the view of clinical applications, an accurate understanding of the hemodynamics could help physicians to achieve better treatment of large aneurysm. As we all know, the hemodynamics is related to the physiological parameters, aneurysm geometry, and parent artery (PA). However, the most extensive simulation studies could not take all factors into consideration. In practice, different geometries would lead to significant differences on final simulation results [4]. Meanwhile, the patients with changing aneurysmal flow patterns were more easily suffered from the aneurysm rupture [5]. Therefore, investigation of the sensitivity analysis of blood flow on hemodynamics becomes essential and important, which has been conducted by only a small number of researchers until now.

In this work we will introduce mass and momentum conservation equations to investigate the hemodynamics in a large unruptured ICA. The effects of different PA segmentation and inflow velocities on hemodynamics are also investigated in terms of intra-aneurysmal flow pattern, total pressure and wall shear stress. The simulation results could illustrate how blood flow patterns change within aneurysms, and assist physicians in improving treatment outcomes in large unruptured ICAs.

2 Method

2.1 Medical Imaging and 3D Geometric Reconstruction

A large unruptured ICA of a 53 year old male was imaged using C-arm X-ray system (Phillips Integris Allura, Phillips Medical Systems, Best, The Netherlands). The images with spatial resolution of 0.5mm in the x, y and z planes were reconstructed

into a 3D dataset of $256 \times 256 \times 256$ voxels on a dedicated Philips Integris workstation. The images, shown in Fig. 1(a), were used to visualize the ICA and PA. The 3D geometry was constructed using a commercial image processing package MIMICS (Materialise, Leuven, Belgium). To investigate the effects of PA segmentation on intra-aneurysmal hemodynamics, we presented two different patient-specific models of ICA and PA in Fig. 1(b).

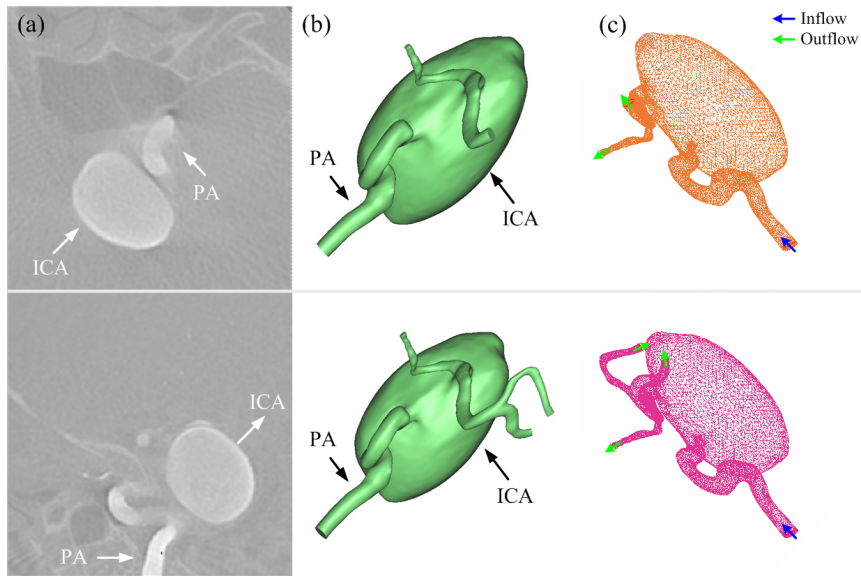


Fig. 1. Medical imaging and 3D geometric reconstruction: (a) front and axial views of the reconstructed images from C-arm X-ray system; (b) two different patient-specific models of ICA and PA; (c) computational surface meshes. Both blue and green arrows indicate the directions of blood flow.

As show in Fig. 1(c), the fluid volumetric meshes were created and defined by ANSYS ICEM (ANSYS, Canonsburg, Pennsylvania, USA) in this paper. For the two aforementioned geometric models, the final fluid volume tetrahedral elements and wall prism elements contained were 205450 and 250082, respectively. To achieve accurate blood flow simulations, the physiological parameters of ICA and PA should be achieved as reliable as possible in practice. In particular, the details of the physiological parameters mentioned in this paper are shown in Table 1.

Table 1. The physiological parameters of ICA and PA

Item	Symbol	Value
Inlet diameter of PA (mm)	Diameter (D)	2.353
Inlet velocity of PA (m/s)	Velocity (U)	0.360
Outlet pressure of PA ($10^4 \times \text{Pa}$)	Pressure (P)	1.250
Length of ICA (mm)	Length (L)	26.47
Width of ICA (mm)	Width (W)	15.04
Height of ICA (mm)	Height (H)	14.03
Density of blood ($10^3 \times \text{kg/m}^3$)	Density (ρ)	1.056
Viscosity of blood ($10^{-3} \times \text{Pa}\cdot\text{s}$)	Dynamic viscosity (η)	3.500

2.2 Mathematical Modeling Hemodynamics

The effect of non-Newtonian behavior was often negligible in medium and large arteries, thus the blood was assumed to be a Newtonian fluid with a density of 1056kg/m^3 and a dynamic viscosity of $0.0035 \text{Pa}\cdot\text{s}$ [6,7] in Table 1. In particular, a steady-state flow condition was applied at the artery inlet, and the pattern of flow was incompressible and laminar [8]. Meanwhile, the rigid-wall boundaries with no-slip conditions at vessel walls were implemented in this paper.

The equations governing the blood flow in large ICA and PA were defined as follows [2]:

1) mass conservation equation:

$$\nabla \cdot \mathbf{u} = 0 \quad (1)$$

2) momentum conservation equation (Navier-Stokes)

$$\frac{\partial \mathbf{u}}{\partial t} + \mathbf{u} \cdot \nabla \mathbf{u} = \frac{1}{\rho} \nabla \cdot [-pI + \eta(\nabla \mathbf{u} + (\nabla \mathbf{u})^T)] \quad (2)$$

where \mathbf{u} is the velocity field, ρ is the blood density, p is the static pressure and η denotes the dynamic viscosity. In particular, the assumption of constant pressure outlet boundary conditions ($P = 12500 \text{Pa}$) was adopted in simulation experiments. The inflow velocity ($U = 0.36 \text{m/s}$) was predefined at the artery inlet. These physiological parameters were directly determined using actual data from the original study [9,10]. To obtain the spatial-dependent fluid field, the governing equations (1,2)

were solved numerically on the computational grid of ICA and PA shown in Fig. 1(c). The patient-specific blood dynamic simulations were implemented using a general purpose CFD solver FLUENT 14.0 with finite volume method. We achieved the final simulation results via the CFD post-processing software.

3 Results

3.1 Effects of Parent Artery Segmentation on Hemodynamics

For PA segmentation analysis, two geometric models are presented in Fig. 1(b). Both of them have the same artery inlet, but one model has two blood outlets; and the other one has three outlets for comparison. The originals of velocity streamlines are placed in the blood flow inlet. From these originals, the streamlines are then generated in both upstream and downstream directions. The physiological parameters used for these experiments are shown in Table 1.

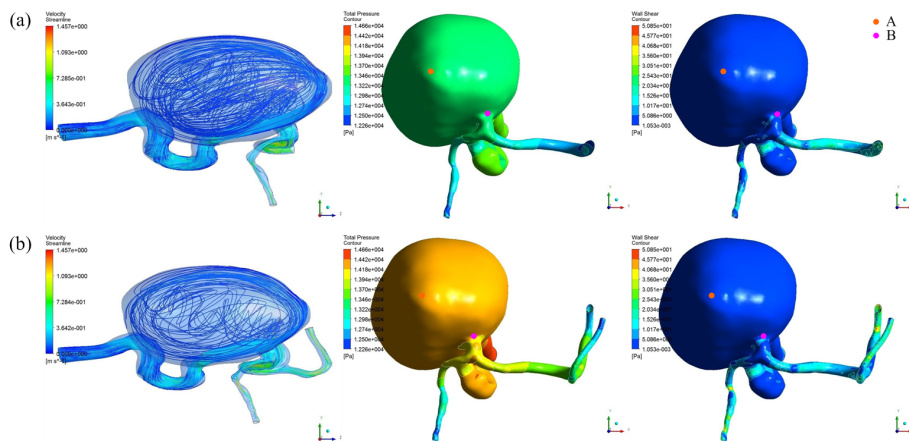


Fig. 2. Computational comparisons of hemodynamics between different PA segmentation results with (a) two blood outlets and (b) three blood outlets. Summary of simulation results (from left to right): velocity streamline, total pressure and wall shear stress.

The simulation results are presented in Fig. 2. This figure displays the distributions of velocity streamlines, total pressure and wall shear stress for two geometric models. From the streamline plotted to visualize aneurysm flow pattern, the pattern is more complex within the aneurysm with two outlets. But there is only a slight difference

between total pressures within two geometric models. In particular, the pressures at points A and B in model (a) are 13358.3Pa and 13339.9Pa, and in model (b) are 14213.8Pa and 14215.3Pa, respectively. In contrast, the effect of PA segmentation on wall shear stress (WSS) is significant near the neck (point B), where the WSS in models (a) and (b) are respectively 1.8485Pa and 4.1595Pa. As shown in Fig. 2, the PA is exposed to a higher WSS compared with aneurysm.

3.2 Sensitivity Analysis of Inflow Velocities on Hemodynamics

In this experiment, we focused on sensitivity analysis of inflow velocities on hemodynamics in terms of intra-aneurysmal flow pattern, total pressure and WSS. To guarantee accurate numerical simulation of blood flow, the more realistic geometry model with three outlets was adopted. The inflow velocities ranged from 0.2m/s to 0.8m/s with step size of 0.2m/s.

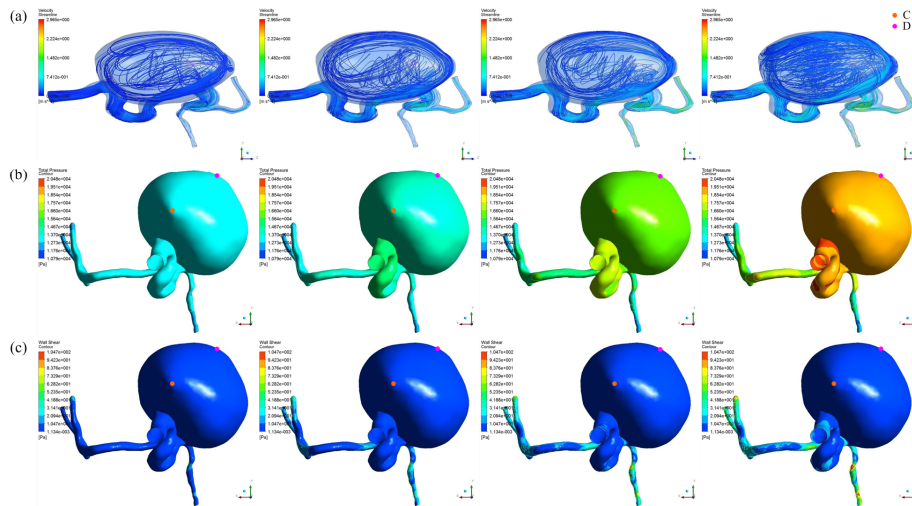


Fig. 3. Computational comparisons of (a) velocity streamline, (b) total pressure and (c) wall shear stress under different assumptions of inflow velocity. From left to right: 0.2, 0.4, 0.6 and 0.8m/s.

Fig. 3 shows the blood flow patterns of four choices of inflow velocities in a more realistic modeling of aneurysm. One can observe that the flow patterns undergo significant changes under different assumptions of inflow velocity. The velocity of the fluid can be represented by the density of streamline. The crowded streamlines

indicate that the fluid velocity is high. As shown in Fig. 3(a), the result is more crowded streamlines when the inflow velocity becomes higher. Thus the streamline in this aneurysm is sensitive to the inflow velocity. The difference in total pressures between different velocities in the aneurysm is significant. In particular, higher inflow velocity results in higher pressure perpendicular to the aneurysmal wall. Take the point C as an example, the total pressure ranges from 13172.6Pa to 18751.4Pa as the velocity increases. The aneurysmal WSS increases with increasing blood flow velocity at point C. In contrast, the velocity 0.6m/s yields the highest WSS (0.4145Pa), and velocity 0.2m/s generates the lowest WSS (0.0434Pa) at point D in the patient-specific geometry model. Thus the velocity streamline, total pressure and WSS are sensitive to the assumption of inflow velocity. It is worth noting that the physiological parameters should be defined accurately and reliably to guarantee the high-quality numerical simulation.

4 Conclusions

In this paper we investigated the blood flow dynamics in a large unruptured ICA that was constructed from C-arm X-ray images. In particular, the objectives of this study are divided into two main parts: (1) effects of PA segmentation on hemodynamics; and (2) sensitivity analysis of inflow velocities on hemodynamics. For PA segmentation analysis, there are significant differences between WSS near the neck within two geometric models. In contrast, limited influence occurs on the WSS distribution within the aneurysm. Meanwhile, only a slight difference between total pressures is generated in this experiment. In the second experiment, the sensitivity of blood flow has been investigated with respect to inflow velocity. Steady state flow simulations illustrated that the velocity streamline, total pressure and WSS are sensitive to the inflow velocity.

In conclusion, in the presented case of a large unruptured ICA, the selection of PA segmentation and inflow velocities plays an important role in blood flow simulation. To guarantee accurate numerical simulations, the patient-specific hemodynamic simulations should be implemented based on accurate and reliable PA segmentation and physiological parameters. In our future work, we plan to investigate the effects of flow diverter stent treatment on hemodynamics in large intracranial aneurysms. The numerical simulation results will be compared with the clinical data of patients treated with flow diverter stent in the postoperative follow-up. In clinical practice, the

hemodynamic investigation can enhance the understanding of aneurysm progression, growth and rupture, and may offer improved results for aneurysm treatment.

Acknowledgement: The work described in this paper was partially supported by a grant from the Research Grants Council of Hong Kong SAR (Project No.: CUHK 416712, 473012), and a grant from the NSFC (Project No. 81201157).

References

1. Raschi, M., Mut, F., Byrne, G., Putman, C.M., Tateshima, S., Viñuela, F., Tanoue, T., Tanishita, K., Cebal, J.R.: CFD and PIV analysis of hemodynamics in a growing intracranial aneurysm. *Int. J. Numer. Method Biomed. Eng.* 28(2), 214-228 (2012)
2. Yu, S.C., Kwok, C.K., Cheng, P.W., Chan, K.Y., Lau, S.S., Lui, W.M., Leung, K.M., et al.: Intracranial aneurysms: midterm outcome of pipeline embolization device—a prospective study in 143 patients with 178 aneurysms. *Radiology* 265(3), 893-901 (2012)
3. Valencia, A.A., Guzmán, A.M., Finol, E.A., Amon, C.H.: Blood flow dynamics in saccular aneurysm models of the basilar artery. *J. Biomech. Eng.* 128(4), 516-526 (2006)
4. Rooij, W.J., Sluzewski, M.: Endovascular treatment of large and giant aneurysms. *AJNR Am. J. of Neuroradiol.* 30(1), 12-18 (2009)
5. Castro, M.A., Putman, C.M., Cebal, J.R.: Computational fluid dynamics modeling of intracranial aneurysms: effects of parent artery segmentation on intra-aneurysmal hemodynamics. *AJNR Am. J. Neuroradiol.* 27(8), 1703-1709 (2006)
6. Müller, J.D., Jitsumura, M., Müller-Kronast, N.H.: Sensitivity of flow simulations in a cerebral aneurysm. *J. Biomech.* 45(15), 2539-2548 (2012)
7. Tremmel, M., Dhar, S., Levy, E.I., Mocco, J., Meng, H.: Influence of intracranial aneurysm-to-parent vessel size ratio on hemodynamic and implication for rupture: results from a virtual experimental study. *Neurosurgery* 64(4), 622-630 (2009)
8. Xiang, J., Natarajan, S.K., Tremmel, M., Ma, D., Mocco, J., Hopkins, L.N., Siddiqui, A.H., Levy, E.I., Meng, H.: Hemodynamic-morphologic discriminants for intracranial aneurysm rupture. *Stroke* 42(1), 144-152 (2011)
9. Zhang, Y., Chong, W., Qian, Y.: Investigation of intracranial aneurysm hemodynamic following flow diverter stent treatment. *Med. Eng. Phys.* 35(5), 608-615 (2012)
10. Ma, X.Q., Wang, Y.S., Yu, F.J., Wang, G.X.: Numerical simulations of the discontinuous progression of cerebral aneurysms based on fluid-structure interactions study. *Sci. China Ser. G.* 53(5), 944-953 (2010)

Development of a System for Endovascular Planning of AAA Interventions

I. Macía^{1,3,5}, J.H. Legarreta^{1,3}, S. Rajasekharan^{1,3}, E. Muñoz², O. Hernández², M. de Blas^{3,4}, J.M. Egaña^{3,4}, and M. Graña⁵

¹ Vicomtech Foundation, San Sebastián - Donostia (Spain)
<http://www.vicomtech.org>

² eMedica S.L. <http://www.emedica.es>

³ Biodonostia Health Research Institute, San Sebastián - Donostia (Spain)
<http://www.biodonostia.org>

⁴ Donostia University Hospital, San Sebastián - Donostia (Spain)
<http://www.hospitaldonostia.org>

⁵ Computational Intelligence Group, Univ. of the Basque Country UPV/EHU (Spain) <http://www.ehu.es/ccwintco>

imacia@vicomtech.org

Abstract. Endovascular repair (EVAR) of Abdominal Aortic Aneurysms (AAA) requires a precise knowledge of the patient anatomy in order to choose or design the appropriate endovascular graft so as to avoid complications during and after intervention. We describe our *eVida Aorta* CTA-based system for EVAR planning, which includes a semi-automatic aorta lumen segmentation and advanced vascular analysis, intuitive 3D visualization tools, quantitative diameter and length estimation following different user-selected workflows and overall an intuitive interface allowing supervision of intermediate analysis and planning steps.

Keywords: aorta, Abdominal aortic aneurysm, AAA, endovascular aneurysm repair, EVAR, planning, endograft, stent, Computed Tomography Angiography, CTA, lumen, segmentation, quantification

1 Introduction

An Abdominal Aortic Aneurysm (AAA) is a localized dilation of the abdominal aorta, due to a weakening and ballooning of the vessel wall, exceeding the normal diameter by more than 50%. Surgery is recommended when the rupture risk is more important than the surgery risk. Current guidelines suggest intervention when the aneurysm diameter is >5.0-5.5 cm.

Endovascular Aneurysm Repair (EVAR) is a minimally invasive alternative to open surgical repair developed in the 1990s [1] involving the development and fixation of a stent-graft via catheterism. This excludes the damaged wall from circulation and creates an intraluminal thrombus which tends to shrink after a successful intervention. The intervention, not absent of risks, is much less

aggressive that open surgery and has significantly lower operative mortality [2]. However, the aneurysm, although excluded, is not eliminated and the technique has its own problems due to wrong fixation, recurrent flow into the thrombus area (endoleaks) or device wear, which may require a re-intervention. It is expected that improved pre-operative planning and patient-specific endograft design may reduce EVAR complications.

Pre-operative planning is performed on the basis of CTA imaging by performing patient-specific measurements (diameters and lengths) which allow the selection of the most suitable endoluminal device from a catalogue. However, the use of fenestrated endografts (f-EVAR) is proliferating, since they provide a better personalization and fixation, specially in cases of complex anatomies. These endografts are fixed suprarenally by providing fenestrations for involved subsidiary arteries in which auxiliary stents are fixed. Sometimes these endografts are designed specifically for a given patient, requiring precise design tools involving the definition of the size and position of the fenestrations based on quantitative image analysis. Apart from a few vascular modules in workstations, such as *Syngo CT Vascular Analysis* (Siemens AG, Erlangen, Germany) or *VessellQ Xpress CT* (General Electric, Fairfield, CN, USA) only very recently similar specific tools have been developed such as the *EndoSize* system (Therenva SAS, Rennes, France) or the *SOVA.evar* OsiriX plugin (SOVamed GmbH, Koblenz, Germany)

We describe our *eVida Aorta* (eMedica S.L., Spain) EVAR planning tool which, based on a preliminary aorta segmentation and vascular analysis allows to perform in a intuitive manner the quantitative measurements necessary for the selection and design respectively of standard and fenestrated endografts. It provides a combination of features not present in other softwares (although some of them exist individually), such as a complete aortic tree segmentation, an automatic centerline extraction with a single seed point, quantitative measurements at any point, three types of planning workflow (non-fenestrated, fenestrated and free), an almost fully 3D planning with visual cues and overall an intuitive user interface which also includes a supervision of the intermediate analysis steps and parameters with visual feedback for quality control of the final results.

2 Segmentation of Aorta and Branches

Lumen segmentation in contrasted images may seem a simple task. However, some difficulties arise when trying to develop a general system without special hardware requirements:

- *Non uniform contrast*: CTA contrast is not uniform along the aorta and branches due to their length which produces an intensity bias in the lumen.
- *Dataset size*: last generation scanners provide hundreds of slices for the volume of interest, which requires a method which is not too computationally expensive.
- *Tortuosity*: tortuosity of branches requires a fully 3D approach for the aorta versus slice-by-slice approaches.

- *Shape variability*: relevant vessels are of different size and the aorta lumen and specially the aneurysm may not locally be regarded as a tubular structure due to its large diameter.
- *Adjacent structures*: some adjacent structures of similar intensity may difficult segmentation, such as vertebrae or calcifications.
- *Noise and artifacts*: i.e. image noise and streak artifacts.

Different extraction methods may be considered for vascular structures [3]. For this application, we discarded centerline-based methods, which make use of multi-scale differential or integral operators, because they are too slow for such large vessels and fail to detect the boundary with precision. Active contours and deformable models were also discarded being computationally expensive and having a complex parameter setting for clinical users. A standard region-growing approach with fixed thresholds did not work due to the mentioned contrast inhomogeneities. Adaptive measurements based on confidence criteria as implemented in [4] were not successful either, since adaptive threshold recalculation was computed each time for even larger regions.

For this purpose, we developed a novel adaptive region-growing approach, which is an improvement of the method described in [5]. The inclusion criteria, based on a lower and upper limit for voxel intensities, is recalculated on the basis of the last voxels included in the segmentation and corresponds to the interval

$$[\tilde{x}(B)(1 - k\tilde{\sigma}(B)), \tilde{x}(B)(1 + k\tilde{\sigma}(B))] \quad (1)$$

where $\tilde{x}(B)$ is the median of the set B , $\tilde{\sigma}(B)$ its median absolute deviation (MAD) and k is a multiplying factor used as parameter. Median-based statistics were used since they are more robust against outliers. Furthermore, a conservative absolute upper threshold was set to prevent possible leaks to adjacent structures such as vertebrae. The approach provides the simplicity and speed of a standard region-growing approach with increased robustness.

3 Vascular Image Analysis

The objective of the vascular image analysis stage is to obtain a set of centerlines that can be the basis for obtaining quantitative diameter and length measurements, and to obtain high level information from the vascular topology.

First, an initial voxel-based set of centerlines is obtained by skeletonization via distance-based homotopic thinning. The resulting skeleton cannot be used directly since centerlines are noisy, due to the sensitivity of these methods to surface irregularities. Spurious branches and loops are also present, due to the non-tubular local nature at some parts of the aorta, but specially in the aneurysm region.

In order to solve these issues and perform high level analysis, such as automatic identification of branches, a vessel graph is created from the raw skeleton. Bifurcation points are identified and assigned a vertex on the graph and centerlines connecting vertices are assigned to edges of the graph. This requires

strategies for exploring the voxel-based skeleton and for grouping adjacent bifurcation points into single vertices.

Centerlines assigned to edges are then pruned, by setting a minimum branch length, and smoothed, by a simple averaging window of small size. Graph loops are identified and removed using a breadth-first-search algorithm where the most tortuous segment is removed in order to resolve the loop.

4 Quantification for Endograft Planning

Quantitative image analysis is performed on the basis of the extracted centerlines (Fig. 1). Length estimation is simple if there are no intermediate branches between the selected points and is performed by accumulating interpolated distances between centerline points. If a bifurcation is present, then the length estimation involves different centerline segments, and these have to be first identified, by using a breadth-first-search graph algorithm. Their corresponding centerline distances are then accumulated to obtain the final length.

Diameter estimation is problematic since the precise extracted section plane may be very sensitive to irregularities in the centerline, some of them not completely solved by the initial smoothing. In order to perform section estimation we locally adjust a third-order B-Spline that interpolates neighbour centerline points at the desired location. This allows us to compute the tangent to the centerline in a robust manner, which defines the local section plane. From this section plane, section boundaries are identified by a ray-casting strategy, outliers removed and the final diameters obtained (max, min, average).

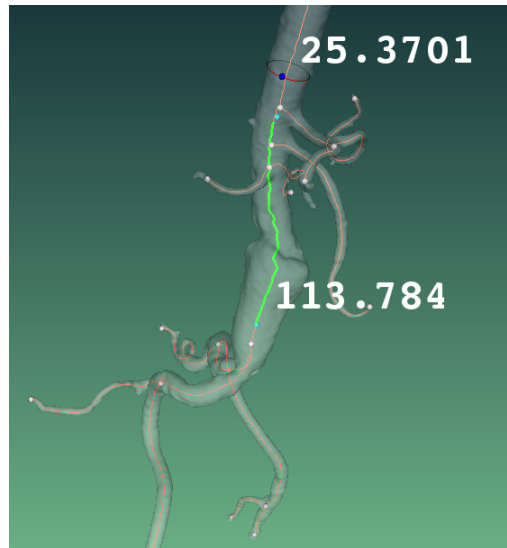


Fig. 1: Centerline-based diameter and length estimation.

5 User Interface

5.1 Segmentation Wizard

The *Segmentation Wizard* (Fig. 2) guides the user through the segmentation and vascular analysis stages. The user interface is intended to be as simple as possible, with minimal and intuitive parameter setting, but allowing for some fine grain control in order to improve the final result. Visual feedback is provided in all the stages for supervision of the intermediate results. The wizard consists on the following stages:

1. *Initialization*: the user is able to select some optional stages, such as VOI selection and image smoothing.
2. *VOI Selection*: reduces computational cost since datasets may be very large.
3. *Image Smoothing*: performs anisotropic smoothing for noisy dataset, but usually is not required.
4. *Lumen Segmentation*: the user selects a single seed point on the first slice. Additionally the user may select the multiplying factor k and the size of the buffer B if the default values are not optimal. Global thresholds may also be set to prevent leaks to adjacent structures, although this circumstance is not common. Segmentation results can be visualized and parameters re-adjusted.
5. *Post-processing*: a dilation of one voxel is usually required to refine the boundary and the user has the possibility of close the gaps up to a given size.
6. *Vascular Analysis*: the vessel graph is created and parameters for pruning and smoothing may be adjusted. The results are shown as 3D models of the aorta lumen and branches and corresponding centerlines.
7. *Conclusion*: resulting segmentation, centerlines and parameters can be saved for later use or directly used in the application.

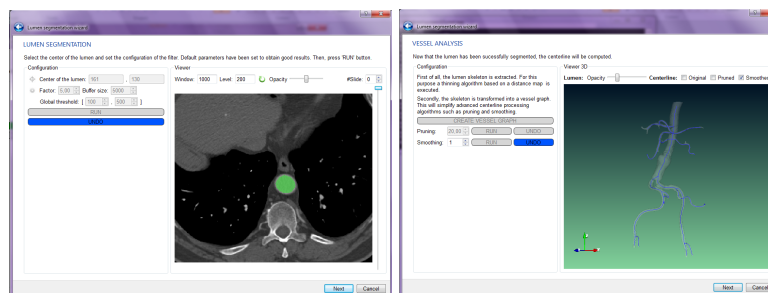


Fig.2: Lumen segmentation (left) and centerline extraction (right) in *eVida Aorta Segmentation Wizard*

5.2 Endograft Sizing and Design

The *Endograft Sizing and Design Module* allows the user to perform the measurements necessary to choose or design an endograft based on the patient specific vascular anatomy. Measurements are performed on a 3D model of the aorta and branches and corresponding centerlines. Different types of planes can be visualized for support, such as MPR planes in 3D space and sections normal to the centerline. The system is also able to reproduce the C-arm rotations.

Length measurements are performed by directly clicking on the surface of 3D model of the aorta at the two desired locations. A highlighted centerline segment is displayed between the selected points. To perform diameter measurements, the user clicks on the 3D model which selects the closest centerline point and displays the estimated section. This position can be adjusted interactively. The estimated diameter is also displayed in a sectional view but the user may choose an alternative diameter interactively. This is useful for example in bifurcations where greater control may be desired. The process is guided by selecting any of three possible workflows:

- *Standard (endograft) mode* (Fig. 3): a standard non-fenestrated endograft is chosen because there is free space for fixation of the device in the infrarenal area. The application guides the surgeon for selecting the points at the aortic neck, bifurcation and iliac arteries and calculates length between these points. Diameters are automatically calculated at 5 and 10 mm. from each of these locations, in order to take into account diameter variations.
- *Fenestrated (endograft) mode* (Fig. 4): fenestrated endografts require the definition of the above standard diameters and lengths plus additional measurements that define fenestrations for the celiac trunk, superior mesenteric artery and renal arteries. Fenestrations are defined by measuring their height as measured from the top of the endograft, clock position and diameters of the fenestration and aorta at that location.
- *Free mode*: the user is allowed to perform any length and diameter measurements and these are recorded accordingly.

Finally, a report is generated with the relevant design parameters and visual information that can be handled to the endograft vendor for fabrication.

6 Initial Validation

One concern in this kind of complex vascular analysis is whether quantitative measurements are reliable and how each intermediate process affects the final result. For this purpose we have developed an initial validation methodology that takes into account the different image processes involved and their parameters, to estimate to which extent they contribute to the length and diameter estimation errors. The methodology is tested in synthetic datasets (i.e. cylinder, volumetric toroid or helix) where the centerlines and diameters are precisely known, since they are generated procedurally, and can be used as ground truth. The complete

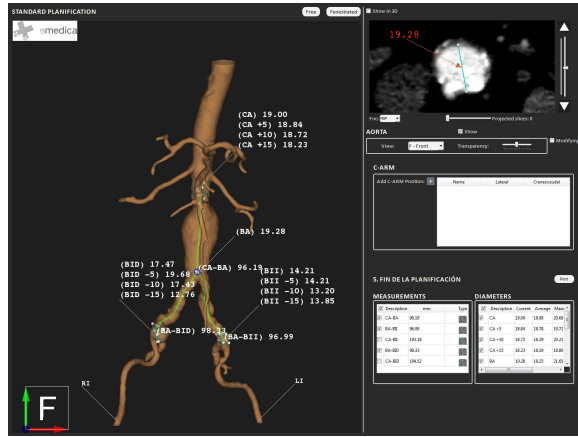


Fig. 3: Non-fenestrated endograft workflow in *eVida Aorta* application.

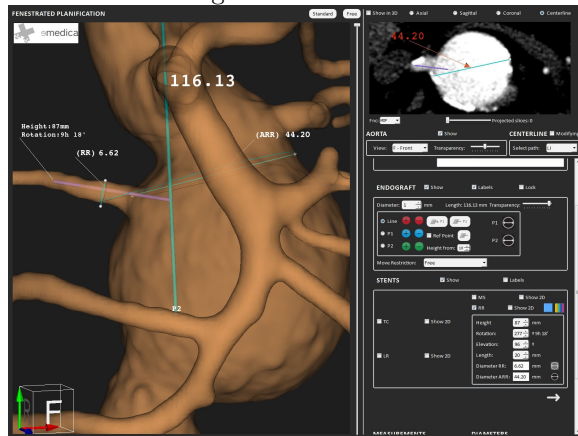


Fig. 4: Fenestrated endograft workflow in *eVida Aorta* application.

process is described in detail in [6], but we enumerate here to the possible sources of errors as a summary of the approach:

- *Segmentation Error*: depends on the segmentation approach. For a successful segmentation we assume an error of about one voxel. Although diameter estimation is performed directly on the source image at sub-voxel precision, the segmentation error affects subsequent processes such as centerline estimation which in turn determines diameter and length.
- *Centerline Error*: depends mainly on the rugosity of the segmented surface, on the image resolution, due to the voxel-wise nature of the extracted centerline, and on the size of the window used for centerline smoothing.
- *Length Estimation Error*: absolute difference in length between the measured and the ground truth length of the extracted centerlines in the synthetic dataset.

- *Diameter Estimation Error*: absolute difference in diameter between the measured and the ground truth diameters at each point of the extracted centerlines.

We tested the influence of image resolution, vessel curvature and centerline smoothing in the final measurements for volumetric cylinders, toroids and helices of different sizes, demonstrating the relevance of obtaining precise and smooth centerlines. Next steps will involve performing similar experiments in simulated and/or real CT data, possibly involving phantoms with known geometry.

7 Conclusions

We have developed the *eVida Aorta* CTA-based system for AAA EVAR planning which is able to guide the user in obtaining relevant vascular quantitative and qualitative information for the design of the most suitable endograft. It performs advanced vascular analysis of the aorta, provides an intuitive 3D visualization and interaction environment and a workflow that guides the user through all the process. The system is centered in providing the necessary usability and robustness, but allowing for supervision of the intermediate steps and results that leaves the final decision in hands of the surgeon.

The system is currently in the process of clinical validation that demonstrates its utility for planning of EVAR interventions. The ultimate long-term goal would be to demonstrate the hypothesis that a better customized stent selection may improve success and long term survival of EVAR interventions. Future work involves further validation, automating some parts of the design process, extending the system to handle the planning of EVAR interventions of Thoracic (TAA) and Thoraco-abdominal (TAAA) aortic aneurysms and trying to simulate the deployment of the designed endograft.

References

1. Schermerhorn, M., O'Malley, A., Jhaveri, A., Cotterill, P., Pomposelli, F., Landon, B.: Endovascular vs. open repair of abdominal aortic aneurysms in the medicare population. *N Engl J Med* **358** (2008) 464–474
2. Investigators, T.U.E.T.: Endovascular versus open repair of abdominal aortic aneurysm. *N Engl J Med* **362** (2010) 1863–71
3. Lesage, D., Angelini, E., Bloch, I., Funka-Lea, G.: A review of 3d vessel lumen segmentation techniques: Models, features and extraction schemes. *Medical Image Analysis* **13**(6) (December 2009) 819–845
4. Ibanez, L., Schroeder, W., Ng, L., Cates, J.: *The ITK Software Guide* 2nd Ed. Kitware, Inc. ISBN 1-930934-15-7. (2005)
5. Macía, I., Graña, M., Maiora, J., Paloc, C., de Blas, M.: Detection of type ii endoleaks in abdominal aortic aneurysms after endovascular repair. *Computers in Medicine and Biology* **41**(10) (Oct 2011) 871–89
6. Arenas, M., Macía, I., Legarreta, J., Graña, M., Rajasekharan, S.: Quantification of abdominal aorta and branches in cta images for endovascular repair of aneurysms: a validation study. In: *Proc. OSA Quantitative Medical Imaging* (to appear). (2013)